Finite Elements in Analysis and Design 134 (2017) 1–15

Contents lists available at ScienceDirect

Finite Elements in Analysis and Design

journal homepage: www.elsevier.com/locate/finel

# Determination of the WYPiWYG strain energy density of skin through finite element analysis of the experiments on circular specimens

Xabier Romero, Marcos Latorre, Francisco J. Montáns*

*Escuela Técnica Superior de Ingeniería Aeronáutica y del Espacio, Universidad Politécnica de Madrid, Pza. Cardenal Cisneros, 28040 Madrid, Spain*

ARTICLE INFO

*Keywords:*
Skin behavior
Finite element analysis
Soft tissues
Hyperelasticity
Anisotropy
WYPiWYG hyperelasticity

ABSTRACT

Skin is a biological material which mechanical behavior has large variations depending on the individual and the location of the specimen in that individual, among other factors. Large differences are also encountered in measurements between *in vivo* and *in vitro* specimens. Then, optimal characterization of the skin for simulation (for example) of surgical procedures requires that all experiments to characterize the material behavior be performed on the same specimen and *in vivo* if possible. Recent experiments on circular discs (Groves et al., 2013 [16]) permit this characterization using a single specimen as we show in this paper, and may constitute a good starting point for ulterior characterization *in vivo*. However, because in these tests deformations are not homogeneous, the determination of the material behavior is not as direct as with tensile or biaxial tests, so finite element analysis is needed to propose a procedure to determine the material behavior. In this work we perform an analysis of the experiments using finite elements obtaining an insight which permits a very simple iterative procedure to determine the stress-strain behavior of the material and, thereafter, the corresponding What-You-Prescribe-Is-What-You-Get (WYPiWYG) stored energy densities.

## 1. Introduction

Skin is the largest organ of the human body, the one with most contact with the environment and which accounts to about the 15% of the body weight [15]. Skin is a very complex organ that has three well-defined and interconnected structural and functional units, namely: epidermis, dermis and hypodermis (from the external surface to the inner surface). In all the units of skin tissues there are cells and extracellular matrix (ECM), mainly collagen, elastin and proteoglycans. Additionally, other specific structures such as blood vessels, nerves, and glands are may be present in certain units. From a mechanical point of view the dermis, and more precisely, the ECM is the component mostly responsible for the observed mechanical behavior.

Mechanical properties of skin have been measured *in vitro* following diverse techniques, see for example [8,3,37,45,17,34,44,50,51,23]. However, even though freezing specimens for conservation does not affect mechanical properties [13], the mechanical behavior of skin has a large variability which strongly depends on the individual and on the location in the body [15,3,17], as well as in the presence of skin pathologies [14]. Mechanical properties also change with the length scale [18], with sex [2], humidity [54,41,18], temperature [41,25,55], overall health condition [15], environmental damage [35], etc. Therefore, it is apparent that for obtaining reliable sets of experimental curves that can be used in the characterization of constitutive models, experiments should be performed in the same specimen or otherwise in the same individual in very nearby locations. Averaging or mixing experimental data from different specimens may result in an unphysical behavior [43] because in fact, the result does not correspond to that of any real, existing material. To this end, *in vivo* testing in preferred. Several techniques have been applied as indentation tests in [40,39], surface waves in [33], air pressure in [7], suction in [19], mechanical movement in [12] also added to digital image correlation in [11], and even in *in vivo* but boundary-free configurations obtained by surgery in [6]. Obviously, although more difficult and more expensive, true biaxial tests are to be preferred in characterizing biological tissues because it allows for the determination of coupling terms in the stored energy function. However, because of the complex anisotropic structure of the skin, all these experiments are difficult to use in developing finite element simulations to model completely the mechanical response of the skin in a general configuration and in a wide range of possible deformations, which is the purpose if finite element simulations of surgery in organs are to be performed.

The experiments of [16] are of special relevance because, even being *ex vivo*, several relatively simple tests are performed on the same specimen. This is thanks to the circular shape of the specimen which allows to test the material in a similar way as it is done for tensile tests but

* Corresponding author.
*E-mail addresses:* xabier.romero@upm.es (X. Romero), m.latorre.ferrus@upm.es (M. Latorre), fco.montans@upm.es (F.J. Montáns).

http://dx.doi.org/10.1016/j.finel.2017.05.009
Received 19 October 2016; Received in revised form 29 April 2017; Accepted 19 May 2017
0168-874X/ © 2017 Elsevier B.V. All rights reserved.

in different directions. We will see herein that despite being nonhomogeneous tests, they can be assimilated to equivalent homogeneous tests, and furthermore, the tissue outside the gauge section has little influence. Thus, an extrapolation of the methodology for *in vivo* testing and then address patient-related simulations seems to be natural and promising. However, the hypothesis of homogeneity of the stress field typically assumed in tensile tests is, in principle, questionable for the tests at hand. In fact, Groves et al. [16] did not consider a homogeneous stress field and performed finite element analysis to develop a complex inverse analysis to determine the parameters of their constitutive model. The use of optimization algorithms and of inverse analyses using finite element meshes are frequent in the biomechanics literature, see for example [5,11,24,52,22] and [1]. In this work we analyze some experiments in Ref. [16] in order to establish a simple methodology which allows us to perform accurate predictions on the behavior observed in the experiments without employing optimization algorithms or material parameters. In contrast to the work of [16] and accepting the current difficulty in developing a structure-based model which accurately accounts for the explained complex multilayer structure of the skin and is still efficient for finite element simulations, we employ herein the new What-You-Prescribe-is-What-You-Get (WYPiWYG) methodology [47,27,28], which has been employed successfully in capturing the behavior of other soft biological materials, see [27,32] and [31]. The procedure herein introduced is intuitive and uses a nonlinear iterative procedure to determine the effective length and effective area from which stress-strain curves may be obtained. These stress-strain curves are captured by the WYPiWYG procedure. Then, the finite element analysis of the experiments predict the load-displacement curves with excellent accuracy. To the best of our knowledge, this type of simple deterministic analysis has not been done in the literature for obtaining the material behavior in soft tissues from nonhomogeneous tests, where the use of costly optimizations, giving non-unique material parameters, is usual.

The rest of the paper is organized as follows. We first briefly review and comment the experiments of Groves et al. [16] to be analyzed herein. Then, in order to explain the ideas in a simple context, we analyze the experimental setting under an isotropic small strains model and an isotropic Ogden model with parameters typical for skin. Thereafter we review the WYPiWYG model and introduce an improvement in the computational algorithm. Afterwards, we explain the iterative process for inverse analysis, perform stress-strain predictions and obtain the resulting load-displacement curves which are compared to those obtained experimentally by Groves et al. [16]. Finally we discuss the approach and make some conclusions.

## 2. Experiments and parameter-fitting procedure from Groves et al. [16]

As mentioned, in [16] a new experimental procedure to characterize soft biological tissues is introduced, and used therein to characterize human and murine skin. The procedure was based on three different tensile tests on circular skin specimens. The use of circular specimens allowed them to conduct the test in the same material, provided that no damage nor permanent deformation is introduced to the specimen.

Human skin samples were obtained from two different donors. Murine samples were obtained from eight donors. For the murine samples equivalent orientations were recorded whilst for human samples these orientations were not recorded. For each specimen, three tensile tests were conducted in directions corresponding to 0°, 45°, and 90°with a common reference, which is the centerline of the back, see Fig. 1. Hence $0^o$ naturally corresponds to a symmetry plane. The corresponding load-displacement curves for each test were obtained. An example of this set of curves is shown in Fig. 2. Special grips were designed in order to hold the skin correctly in the tensile tests and applying a constant pressure in the jaw faces during the test. The maximum load in the tests was limited to ensure that no permanent damage occurred to the samples.

A further study on the mechanical properties of the skin was conducted by the authors based on the data retrieved from the tests. An anisotropic structure-based hyperelastic model was chosen to characterize the hyperelastic response of the skin. The material behavior was modeled using three layers of transversely isotropic hyperelastic material with a different family of fibers for each layer. For each layer the strain energy function was written as a function of the classical invariants, the stretch in the fibers and the jacobian determinant, as

$$\Psi = F_1(I_1, I_2) + F_2(\lambda) + \frac{K}{2}(\ln J)^2 \tag{1}$$

where $F_1(I_1, I_2)$ corresponds to the isotropic matrix modeled by Veronda and Westmann [49]. The families of fibers were modeled based on the stretch of the fibers $\lambda$ as indicated by the contribution $F_2(\lambda)$ proposed by Weiss et al [53].

The parameters were fitted for each specimen using optimization to reproduce as close as possible the experimental results. A finite element model with the material was implemented in order to reproduce the tests. Few computational details are given about the actual minimization procedure followed during the simulations. They report that the optimization procedure followed the Simplex algorithm connected to finite element analysis and that the maximum number of iterations allowed were 1500. The authors report that the optimization procedure presented great sensibility to the changes in the parameters and that only a local minimum is obtained, a frequent observation found in other works employing optimization procedures for determination of material parameters in soft materials, and that will not be present in our analysis. The authors include a volumetric term, but the associated bulk modulus is not given nor included in the optimization procedure, probably because the material is assumed quasi-incompressible and, hence the specific value is usually irrelevant for the purpose. The finite element mesh was made of standard solid elements.

The disc dimensions were assumed constant. The diameter of the disc was 31 mm and the thicknesses were assumed 1.86mm and 0.265mm for the human and murine skin, respectively. Clamps were modeled using contact in an area of $15 \times 2\text{mm}^2$. Even though the constitutive model may result in a strongly anisotropic behavior, the authors used only one quarter of the disc in order to save computational time in the probably very time consuming optimization procedure. Because in our work the computational times are small, we do not need to take this simplification and, hence, we have considered the full disc. However, despite that simplification (justified below by computational results) Groves et al [16] report excellent fittings for all three tests in skin from all donors.

## 3. Comparison of rectangular specimens and circular specimens

The circular specimens introduced in the tests [16] differ from the rectangular specimens used to characterize the constitutive behavior in uniaxial tension of tissues. In uniaxial tests of metals it is typical the use of specimens with gauge length-to-width ratios of 4, see for example 4:1 for rectangular specimens in the US ASTM:E8 standard [4] and in the ISO [20] one. Grip distance-to-width ratios are even larger, orders of 7:1 are usual [20]. These aspect ratios are required in order to be able to consider uniaxial test boundary conditions and uniform deformations in the cross section. An experimental study on the strain distributions in metals along the gauge length [42] showed that for a 4:1 ratio this distribution was uniform over an 80% of the width in the central section of the gauge length. However, for the circular specimens used [16] the gauge section presents a ratio of 1:1, i.e. the ratio of the distance between clamps (15 mm) to the width of the clamps (15 mm). Within the small strain regime, one should not expect a uniaxial stress state in the central cross-section of circular specimens, but in the nonlinear regime the situation may change. Indeed, the particular nonlinear response that skin exhibits gives as a result a transverse behavior

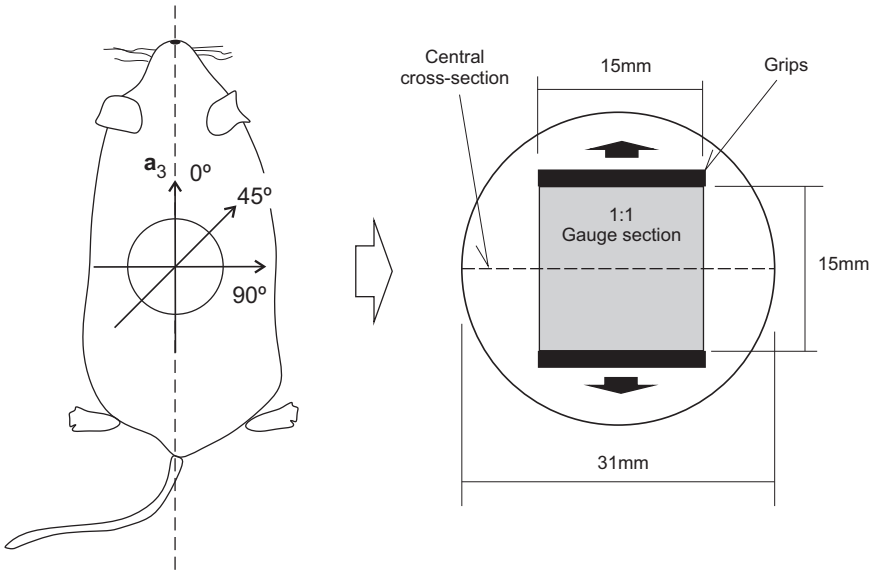


**Fig. 1.** Experiments of Groves et al. [16] on murine skin: orientation and layout of the specimens.

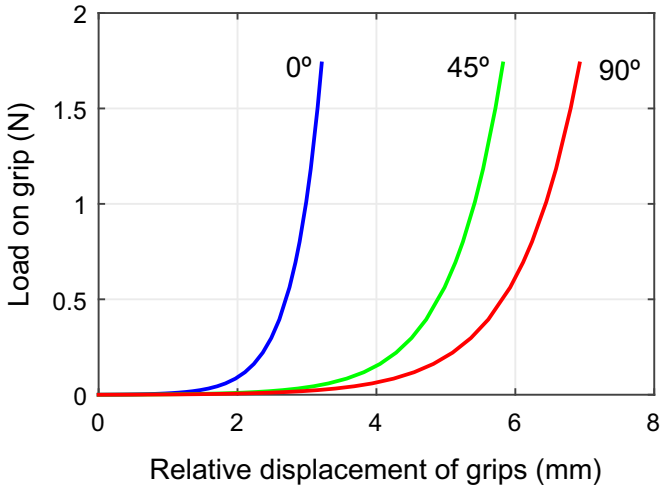


**Fig. 2.** Experimental load-displacement curves after [16] (Fig. 5a Anterior). Blue, green, and red correspond to measurements at 0°, 45° and 90°, respectively. (For interpretation of the references to color in this figure legend, the reader is referred to the web version of this article.)

in the tests which is different from the transverse behavior obtained within the linear range. This important observation will allow us to consider lower *uniaxial* specimen ratios than the ones recommended in [4,20,42]. Furthermore, it will be seen in the finite element simulations in discs that the material outside the 1:1 gauge section has little influence in the observed load-displacement behavior. This section focuses on the comparison of rectangular specimens with circular specimens and also on the influence of the stress-strain response of the skin in both tests through both analytical calculations and finite element simulations.

### 3.1. An analogy: the bilinear model

The main difference between a high length-to-width ratio specimen and a low length-to-width ratio specimen, both subjected to uniaxial loading, is the transverse response in their respective central cross-sections. Conventional materials undergo positive transverse contraction (i.e. negative transverse strains) under simple tension tests and the same obviously holds for at least some biological tissues, see [46]. Hence, the compression part of the strain energy function being considered is being assessed even in uniaxial *tensile* tests. Its consideration becomes extremely important when the corresponding strain energy density is being determined from experiments and may explain very important issues frequently encountered in the literature from lack of uniqueness and lack of convexity of the hyperelastic models determined from tensile tests, see [26]. From a purely academical standpoint, we may study the *non-linear finite-strain* behavior of biological tissues under uniaxial loadings, in which the compression branch is present and which may be different to the tension branch, through a *bi-linear small-strain* model with different behavior in tension and compression. For the matter of simplicity in the exposition, we consider isotropic constitutive laws in the present analysis, but the conclusions apply to the anisotropic case.

Consider the following distortional strain energy function—$\varepsilon_1$, $\varepsilon_2$ and $\varepsilon_3$ stand for the isochoric principal engineering strains

$$\mathcal{W}(\varepsilon_1, \varepsilon_2, \varepsilon_3) = \omega(\varepsilon_1) + \omega(\varepsilon_2) + \omega(\varepsilon_3) \tag{2}$$

with $\omega(\varepsilon)$ being piecewise bi-quadratic—we say that the model is bi-linear because the stress-strain response is bi-linear, as we see below

$$\omega(\varepsilon) = \begin{cases} \mu_c \varepsilon^2 & \text{if} \quad \varepsilon < 0 \\ \mu_t \varepsilon^2 & \text{if} \quad \varepsilon \geq 0 \end{cases} \tag{3}$$

where we use the subscripts $c$ and $t$ to refer to compression and tension, respectively.

The (principal) Cauchy stresses that directly derive from the stored energy of Eq. (2) are—we consider the material as perfectly incompressible

$$\sigma_1 = \omega'(\varepsilon_1) + p \tag{4}$$

$$\sigma_2 = \omega'(\varepsilon_2) + p \tag{5}$$

$$\sigma_3 = \omega'(\varepsilon_3) + p \tag{6}$$

where $p$ is an initially undetermined pressure-like variable to be determined from the boundary conditions of the specific test under study (from a mathematical point of view, $p$ is the Lagrange multiplier associated to the incompressibility constraint $\varepsilon_1 + \varepsilon_2 + \varepsilon_3 = 0$). We consider herein that the face which normal direction is direction 3 is stress-free, so $\sigma_3 = 0$ and the previous in-plane equations reduce to

$$\sigma_1 = \omega'(\varepsilon_1) - \omega'(\varepsilon_3) \tag{7}$$

$$\sigma_2 = \omega'(\varepsilon_2) - \omega'(\varepsilon_3) \tag{8}$$

In the present analysis, direction 1 will represent the loading direction,

direction 2 will represent the transverse direction and, as mentioned, direction 3 will be the normal (through the thickness) direction.

In a rectangular specimen with a high enough gauge aspect ratio (e.g. 4:1 or higher), it may be considered that the transverse contraction in the central cross-section is not restricted at all because the lateral restriction effect caused by the grips is far enough. Hence reaction stresses $\sigma_2$ are not present in the central section and the stress-strain response is effectively *uniaxial*. For a tensile load in direction 1 ($\sigma_1 = \sigma_u > 0, \sigma_2 = \sigma_3 = 0$, with subindex $u$ indicating uniaxial test) we obtain

$$0 = \omega'(\varepsilon_2) - \omega'(\varepsilon_3) = 2\mu_c\varepsilon_2 - 2\mu_c\varepsilon_3 \tag{9}$$

$$\Rightarrow \quad \varepsilon_2 = \varepsilon_3 = -\varepsilon_1/2 < 0 \tag{10}$$

and

$$\sigma_u = \omega'(\varepsilon_1) - \omega'(\varepsilon_3) = 2\mu_t\varepsilon_1 + \mu_c\varepsilon_1 \tag{11}$$

$$= (2\mu_t + \mu_c)\varepsilon_1 \quad \text{with} \quad \varepsilon_1 > 0 \tag{12}$$

In a specimen with a low aspect ratio – e.g. a square specimen or a circular specimen with an equivalent rectangular test area with aspect ratio of 1:1 as that of [16] – the transverse contraction in the central cross-section is restricted to some extent because the grips are close to that section and the lateral restriction effect caused by them (and also by the extra material outside the main testing surface if we consider the circular specimen) cannot be neglected. Reaction stresses $\sigma_2 > 0$ appear in the central section as a consequence and the stress-strain response is no longer uniaxial. In this analytical study case, we consider for now the most unfavourable situation in which the transverse deformation is fully restricted, i.e. $\varepsilon_2 = 0$. The conclusions raised for this limit case will be applicable (to a greater extent indeed) to the real case for which $-\varepsilon_1/2 < \varepsilon_2 < 0$.

For a tensile load in direction 1 in the *fully restricted* case ($\sigma_1 = \sigma_{fr} > 0, \varepsilon_2 = 0, \sigma_3 = 0$ with subindices *fr* indicating fully restricted, plane strip test) we obtain

$$\varepsilon_2 = 0 \quad \Rightarrow \quad \varepsilon_3 = -\varepsilon_1 < 0 \tag{13}$$

and

$$\sigma_{fr} = \omega'(\varepsilon_1) - \omega'(\varepsilon_3) = 2\mu_t\varepsilon_1 + 2\mu_c\varepsilon_1 \tag{14}$$

$$= (2\mu_t + 2\mu_c)\varepsilon_1 \quad \text{with} \quad \varepsilon_1 > 0 \tag{15}$$

We observe that $\sigma_u < \sigma_{fr}$ for a given $\varepsilon_1 > 0$. It is straightforward to obtain that in an actual *restricted* case the axial stresses $\sigma_r$ in direction 1 are such that $\sigma_u < \sigma_r < \sigma_{fr}$. Furthermore, in general $|\varepsilon_1| \geq |\varepsilon_3|$.

We now take advantage of the analogy between the non-linear response of skin and this bi-linear model. The axial stiffness (with "stiffness" we refer to second derivatives of the strain energy) that these biological tissues present for large extensions in the test direction (i.e. positive strains) is usually much higher than the stiffness in the transverse direction (i.e. negative strains, either restricted or free). We can elucidate the consequences of that specific behavior just considering $\mu_c \ll \mu_t$ in the foregoing bi-linear analysis. In such a case, the uniaxial tensile stresses of Eq. (12) are

$$\sigma_u = (2\mu_t + \mu_c)\varepsilon_1 \simeq 2\mu_t\varepsilon_1 \quad \text{with} \quad \varepsilon_1 > 0 \tag{16}$$

and the axial tensile stresses of the fully restricted case of Eq. (15) are

$$\sigma_{fr} = (2\mu_t + 2\mu_c)\varepsilon_1 \simeq 2\mu_t\varepsilon_1 \quad \text{with} \quad \varepsilon_1 > 0 \tag{17}$$

Since $\sigma_u < \sigma_r < \sigma_{fr}$, we note that the axial tensile stresses $\sigma_r$ in an actual *restricted* case are also $\sigma_r \simeq 2\mu_t\varepsilon_1$.

Thus, the main conclusion of this section is that, for materials fulfilling the hypothesis of much larger stiffness in tension than in compression, the lateral restriction effect does not modify, in practice, the axial stresses during a non-uniaxial tensile test. Note that in the general nonlinear case, specially in soft biological tissues presenting the typical J-shaped stress-strain curve, since $|\varepsilon_1| > |\varepsilon_3|$, this will happen at large strains even if tension and compression branches are symmetric. Then, we will be able to approximate the axial stresses $\sigma_r$ in the central cross-section of skin circular specimens (with an equivalent rectangular aspect ratio of 1:1) as if they were uniaxial stresses, i.e. $\sigma_u \simeq \sigma_r$. In other words, *we can consider circular specimens as uniaxial specimens*. The additional consideration of an effective reference cross-sectional area, due to the fact that the specimen is circular and not a perfect square, will allow us to obtain the strain energy density of the skin following a very simple, intuitive, engineering-based procedure.

Finally, considering the case $\mu_t = \mu_c = \mu$ in the previous fictitious bi-linear model we recover the actual linear deviatoric strain energy function, for which $\omega(\varepsilon) = \mu\varepsilon^2$ presents a continuous second derivative (stiffness) value in the origin, i.e. the reference Lamé parameter $\mu$. In that case, the uniaxial tensile stresses of Eq. (12) are

$$\sigma_u = 3\mu\varepsilon_1 \tag{18}$$

and the axial tensile stresses of the fully restricted case of Eq. (15) are

$$\sigma_{fr} = 4\mu\varepsilon_1 \tag{19}$$

so $\sigma_u \neq \sigma_r \neq \sigma_{fr}$, which in turn explains why specimens with low aspect ratio cannot be regarded as uniaxial ones in the small strain (linear) regime. These observations are also illustrated in the next section, where we perform finite element analyses of these non-homogeneous deformation states.

### 3.2. Finite element analysis: linear and Ogden models

As mentioned, skin has a particular uniaxial behavior at the continuum level [8,10]. Specifically, three stages can be differentiated. In the first one, the stiffness is low and is followed by a highly nonlinear stage where stresses grow rapidly. The response is linear again with the displacement during the third stage. This characteristic stages can also be observed in the load displacement curves in Fig. 2. This particular behavior induces large (exponential-type) variations in the tensile stresses. This behavior suggests our hypothesis discussed above, i.e. that the stress (and local stiffness) in the testing direction of a circular specimen loaded in tension is much higher than the stress (and local stiffness) in the transverse direction, so the resulting stress state in the central cross-section of the specimen may be considered almost uniaxial, similar to the case of metals for ratios greater or equal than 4:1 (where transverse strains evolve freely and transverse reaction stresses vanish in practice).

To illustrate this observation, finite element simulations have been conducted in the general-purpose commercial finite element code ADINA. Rectangular specimens of 1.86 mm thick, 15 mm width and varying length of 15 mm (1:1 aspect ratio) and 60 mm (4:1 aspect ratio) were analyzed using a linear elastic and a skin representative Ogden material. In this analysis, the X direction corresponds to width (principal direction 2 above), Y to thickness (principal direction 3 above) and Z to length (principal direction 1 above). One of the edges was clamped as boundary condition (displacements restricted in the three degrees of freedom) and the load was applied at the other edge imposing the displacement in the loading direction (Z) and constraining the remaining displacements. The elements used in all the simulations in this paper are fully integrated 27-node tri-quadratic finite elements with mixed $u - p$ formulation and linear pressure to prevent volumetric mesh locking and reproduce adequately possible shear deformations. A nearly-incompressible behavior is enforced through a penalty volumetric stored energy of the form

$$\mathcal{U}(J) = \tfrac{1}{2}K(J-1)^2 \tag{20}$$

where $J$ is the Jacobian determinant of the deformation gradient and $K = 10^8$Pa is the penalty parameter (i.e. the equivalent bulk modulus), high enough to guarantee quasi-incompressibility in all the computational domain, still avoiding numerical conditioning problems. For the

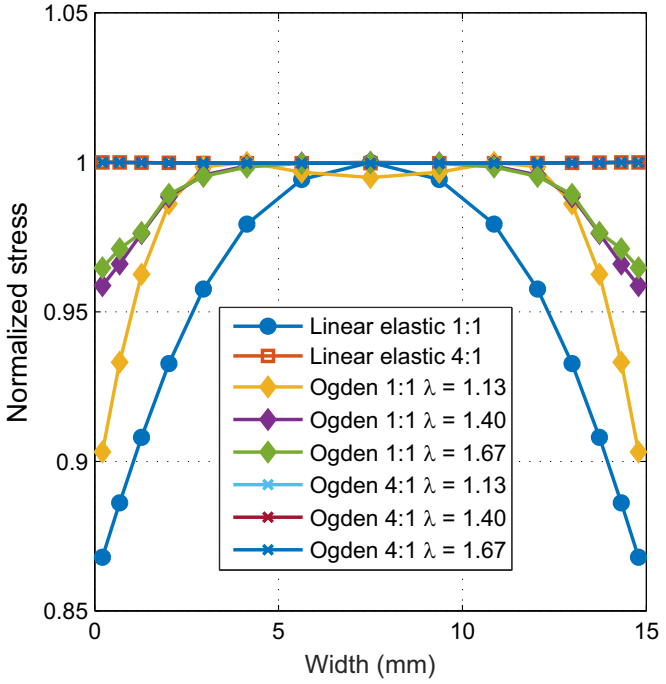


**Fig. 3.** Stress distributions in the uniaxial tests for the rectangular specimens for different aspect ratios, materials and levels of strain.

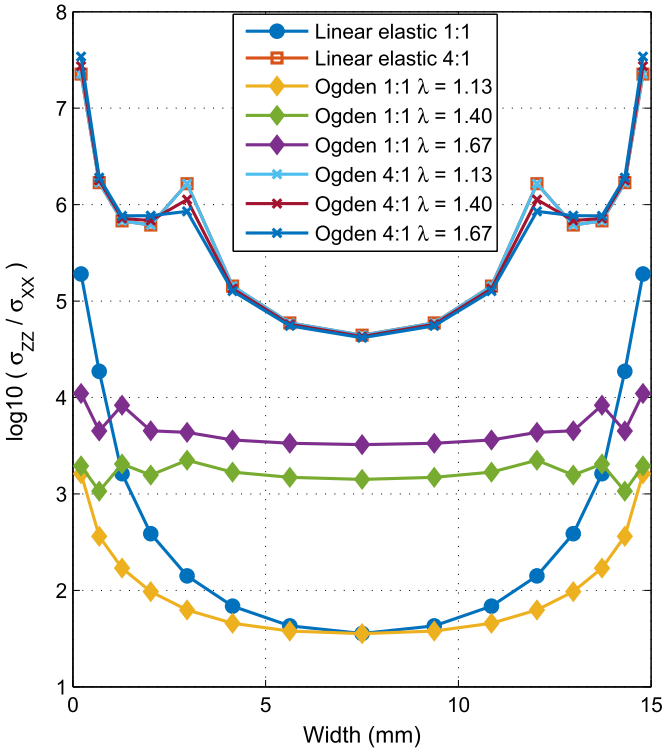


**Fig. 4.** Order of magnitude of the ratio in the stress distributions in the load direction and the transverse direction in the uniaxial tests for the rectangular specimens for different aspect ratios, materials and levels of strain.

linear elastic material the parameters we used are $E = 1$Pa and $\nu = 0.3$ and we imposed an engineering deformation of 1%. The strain energy density for Ogden's model is given by [38]

$$\mathcal{W}(\lambda_1, \lambda_2, \lambda_3) = \sum_{p=1}^{N} \frac{\mu_p}{\alpha_p}\left(\lambda_1^{\alpha_p} + \lambda_2^{\alpha_p} + \lambda_3^{\alpha_p} - 3\right) \tag{21}$$

where $\mu_p$ and $\alpha_p$ ($p$=1,...,$N$) are material parameters. For this analysis, skin was modeled using only $N$=1, $\mu = 10$ Pa and $\alpha = 26$ following the values obtained from experiments in [11]. For the linear elastic material, a small strain framework was considered while for the Ogden material large strains up to stretches of $\lambda = 1.67$ were studied. In the linear case, only one level of strain was considered for obvious reasons, while for the Ogden case the influence of strain level was evaluated accordingly.

From the simulations, the stress distributions along the width of the rectangular specimens were extracted for a cross section located in the middle of the length of the specimen, see Fig. 1. The distributions of stresses in the loading direction $\sigma_{zz}$ normalized with the maximum stress are plotted in Fig. 3. For the linear elastic case, results show that stresses are uniform along the width of the sample for the 4:1 aspect ratio. However, if the aspect ratio is reduced to 1:1 there is a peak variation of parabolic aspect for the stresses along the width. The effect is due to the proximity of the clamps to the central zone, which introduce a transverse restriction that vanishes for the 4:1 aspect ratio. Remarkably, for the Ogden model the distributions obtained present a flat area for the 1:1 case. For increasing strain levels, where the effect of the nonlinear behavior is higher, this distribution becomes flatter. In the region close to the edges the difference with the maximum also becomes smaller as the stretch increases. In the 4:1 aspect ratio, results are similar to the linear elastic material, where the effect of the larger length predominates.

Once the flat stress distribution was confirmed for the Ogden representative material, the uniaxial tension hypothesis is analyzed. The difference in the order of magnitude between the stress in the testing direction $\sigma_{zz}$ and the transverse direction $\sigma_{xx}$ is indicated in Fig. 4. Note that the difference in orders of magnitude is represented through the logarithm. For most configurations the difference is larger than 3 orders of magnitude in the central section of the specimen (i.e. the cross-section at half the distance between grips). The lowest differences, between 1 and 2 orders of magnitude, appear for the 1:1 linear elastic specimens and for the smallest strain of the 1:1 Ogden model, where the linear material behavior predominates. An increase in the strain in Ogden's model implies that there is a higher difference between the axial (tension) and the transverse (compression) stiffness. This observation is in line with the stress-strain nonlinear behavior of skin. When the aspect ratio is increased to 4:1, the difference is even higher. These results confirm the uniaxial tension in the specimens. As a consequence, for materials presenting this type of highly nonlinear tension-compression responses, tests conducted on 1:1 samples can be suitable for characterizing the stress-strain response directly using an appropriate equivalent area as defined later in this section (due to the actual circular shape).

Once the suitability of 1:1 aspect ratio specimens for this type of tissues has been acknowledged, the analysis is extended to circular specimens. The main advantage of using circular specimens instead of rectangular ones is that different directions can be tested in the same sample to characterize anisotropic behavior. As mentioned, the use of the same specimen is remarkably important in biological tissues in general, and skin in particular, given the variability of the properties along samples.

A finite element model of the disc was created in ADINA. The diameter of the disc is 31 mm and its thickness is 0.265mm. The loads and boundary conditions imposed are indicated in Fig. 5. A displacement load was imposed in the volume under the clamps. This differs from the model by Groves et al. where contact was introduced, but this difference is not relevant for conclusions raised in this work.

Similar results to those of the rectangular specimens are analyzed. The stress distribution in the direction of testing (global axis Z) in the mid plane (global XY plane, see Fig. 5) of the circular specimen is plotted in Fig. 6 for varying displacement between clamps $u$. The results indicate that the stress curves are flat in the central section of the specimen. In this case, despite the aspect ratio of the gauge zone

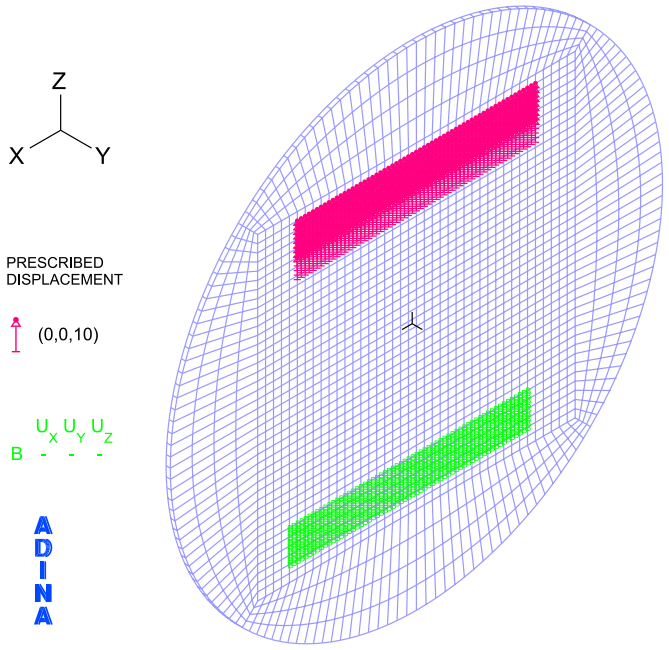


**Fig. 5.** Finite element model of the skin disc used in ADINA. Loads, boundary conditions and global axes orientation.

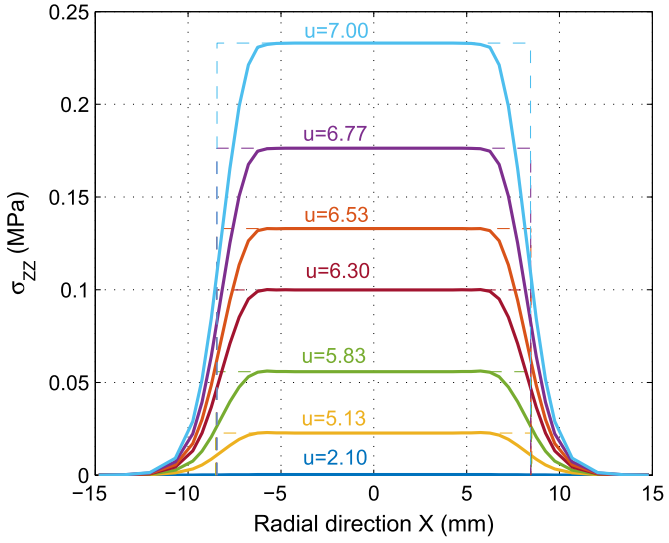


**Fig. 6.** Cauchy stress distribution over the undeformed central section width for the circular specimen samples using an Ogden material model for varying displacement between clamps $u$. Distance between vertical dashed lines represent the effective reference width of the disc $w_{eff}$ for axial loading, i.e. the width of a rectangular uniaxial specimen with the same thickness $h$ that would give equivalence of applied loads during tensile loading. We note that $w_{eff} \approx 16.5\text{mm} > 15\text{mm} = w_{clamp}$ due to the presence of the extra surrounding material in the circular specimen.

being 1:1, the nonlinear material behavior results in a flat distribution as in the cases of 4:1 for linear elastic materials. From the simulation it was verified that the stretch in the central element of the specimens presents good agreement with the strain calculated using the relative displacement of the clamps and the distance between the edges of the clamps (15 mm). The corresponding stress distribution for the disc is represented in Fig. 7. It is clearly seen in the figure that the load path is concentrated in the central square region of the specimen and that the lateral restriction is small.

The stress distributions for the disc shown in Figs. 6 and 7 suggest the definition of an *effective area* for the tensile test. The purpose of the definition of this area is to relate directly the loads and the stresses in the model. For a rectangular sample with aspect ratio equal or larger to 4:1 it can be observed that the stresses in the cross sectional area are constant. However, in the disc the lateral boundaries of the ideal rectangular loading path (gauge section) are not free, but constrained by the behavior of the surrounding material. Nonetheless, the effect of the nonlinearity of the material described with the rectangular samples is also present.

Using the calculated stress distributions in the mid plane of the circular specimen, the effective area is defined as the rectangular cross-sectional area that a uniformly stressed *uniaxial* specimen with the stress in the mid plane would have to result in the same reaction, i.e. integral of the nominal stress distribution over the undeformed central cross-section. This area $A_{eff}$ is expressed as

$$A_{eff} = \frac{1}{P_{uni}} \int_A P dA = \frac{F}{P_{uni}} \tag{22}$$

where $P$ is the nominal (first Piola–Kirchhoff) axial stress distribution in the direction of the test (Z-direction), $P_{uni}$ is the nominal stress in the center of the specimen (taken as the stress of the equivalent uniaxial specimen), $A$ is the disc cross-sectional area in the reference configuration and $F$ is the applied load. Since the stretch $\lambda$ in the loading direction is uniform in the central (loaded) region of the mid plane XY, we can alternatively compute the reference effective area in terms of the distribution of axial Cauchy stresses $\sigma = P\lambda$ within the mid plane

$$A_{eff} \simeq \frac{1}{\sigma_{uni}} \int_A \sigma dA \tag{23}$$

The calculated effective widths $w_{eff} = A_{eff}/h$, where $h = 0.256\text{mm}$ is the thickness of the sample, for the Ogden material model are plotted as dashed lines for the different loads (displacement between clamps) in Fig. 6. Remarkably, the results shown in Fig. 6 demonstrate that, in practice, the equivalent cross-sectional area is almost constant regardless of the load level in this case. This observation is very important because it means that *the concept of effective area gives a unique value valid at all stress levels and it may be considered as a geometric characteristic of the specimen*. Furthermore, the stress distributions given in Fig. 6 indicate that the most relevant part in the behavior is the zone of the specimen within the gauge section, an observation which is relevant for *in vivo* testing.

## 4. WYPiWYG transversely isotropic hyperelasticity

As mentioned in the Introduction Section, the approach developed by [16] is relatively frequent in biological tissues and relies on a parametric fitting of the hyperelastic model following optimization algorithms and using an inverse iterative procedure with finite element analyses. We describe herein an alternative procedure that uses a phenomenological hyperelastic model based on the What-You-Prescribe-is-What-You-Get philosophy. As a main difference with classical models, WYPiWYG hyperelasticity models do not follow any optimization procedure in order to determine the model parameters from experimental data fittings. In fact, WYPiWYG models do not have explicit material parameters. Instead, solution points of the strain energy function decomposition being proposed are exactly calculated (i.e. to any required precision) from experimental data points and then interpolated using cubic splines. As a result, the spline-based representation of the strain energy density function exactly reproduces the experimental data points being initially prescribed. The incompressible isotropic model [47] was generalized for transverse isotropy [27] and orthotropy [28], and for compressible isotropic materials as well [9]. An interesting feature of these models is that they need the same number of curves to determine the energy function as the number of independent constants needed to define the associated infinitesimal model. For example, one complete uniaxial curve (containing two tension-compression independent branches) is required for the incompressible isotropic material, three curves (containing five independent branches) for the transversely isotropic model and six curves

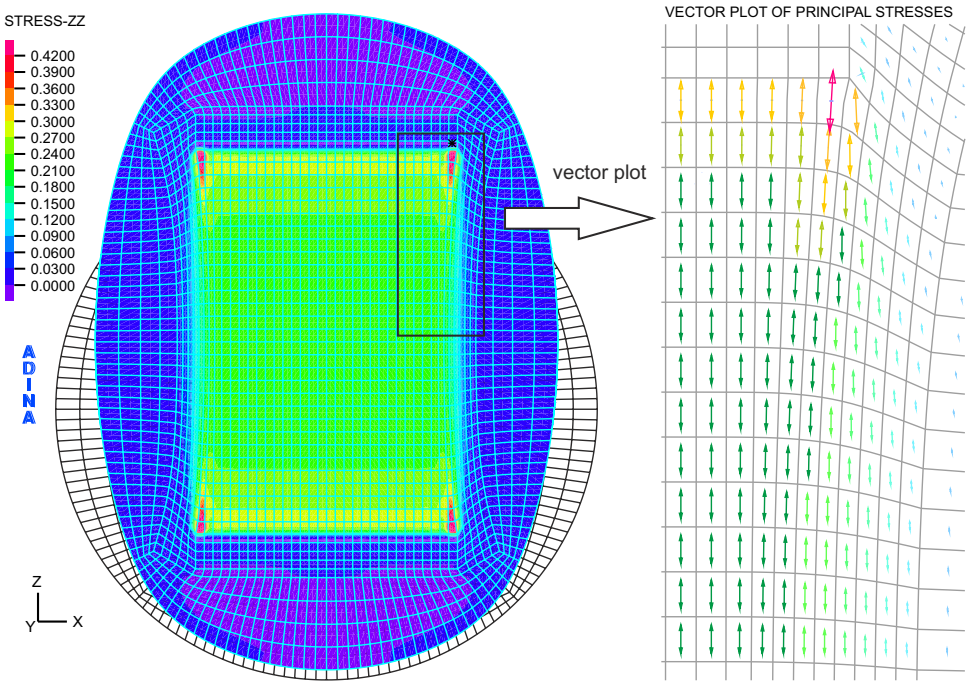


**Fig. 7.** Left: Typical $\sigma_{zz}$ stress distribution (in MPa) for the disc using Ogden's model. Right: close-up of the zone near the grips, showing the principal stress vectors. Note that the stress state can be considered uniaxial in most of relevant zone of the specimen.

(containing 9 independent branches) for the orthotropic one.

The experiments described in Section 2 provide three load-displacement tensile curves which can be reproduced using the transversely isotropic model. Since we are interested in the in-plane behavior, we consider the deviation from isotropy, and there is a symmetry at $0^o$ (centerline of the back), the transversely isotropic model seems a reasonable assumption, and in any case a good approximation. If we had additional tests, the orthotropic model could be equally used, maintaining the same accuracy. We will describe in Section 5 below how to obtain the stress-strain curves, required as input data for the model determination, using: the actual load-displacement curves from the experiments, finite element calculations and the uniaxial response hypothesis discussed above. Previously, in this section we enhance the WYPiWYG procedure presented originally in [27] and also explain how to determine the strain energy shear term using stress-strain data from a uniaxial tensile test performed about a direction at 45°with respect to the anisotropic axis.

### 4.1. Transversely isotropic model description

WYPiWYG transversely isotropic incompressible hyperelasticity is formulated in terms of the components of the isochoric logarithmic strain tensor $\mathbf{E}$ in a preference frame $X_{pr} = \{\mathbf{a}_1, \mathbf{a}_2, \mathbf{a}_3\}$, where $\mathbf{a}_3$ is the anisotropic direction and $\mathbf{a}_1$ and $\mathbf{a}_2$, that define the isotropic plane, are in-plane *principal* directions in the sense that the in-plane shear strain component $E_{12} = \mathbf{a}_1{\cdot}\mathbf{E}{\cdot}\mathbf{a}_2 = 0$ vanishes. The deviatoric strain energy function is

$$\mathcal{W}(\mathbf{E}, \mathbf{a}_3) = \omega_{11}(E_{11}) + \omega_{11}(E_{22}) + \omega_{33}(E_{33}) + 2\omega_{13}\big(E^{\#}_{13}\big) \tag{24}$$

where $E_{33} = \mathbf{a}_3{\cdot}\mathbf{E}{\cdot}\mathbf{a}_3$ is the invariant in the preferred direction, $E_{11}$ and $E_{22}$ are the in-plane principal logarithmic strains (invariants also), and the invariant $E^{\#}_{13}$, accounting for the out-of-plane shearing, reads—note that $E^{\#}_{13} = E_{13}$ for the pure shear and simple shear cases discussed in [27], given that $E_{23} = 0$ in both cases

$$E^{\#}_{13} = \sqrt{E^2_{13} + E^2_{23}} \tag{25}$$

It is readily shown that $E^{\#}_{13}$ can be computed in any *preferred* reference frame $X'_{pr} = \{\mathbf{a}'_1, \mathbf{a}'_2, \mathbf{a}_3\}$ being coaxial with the anisotropic direction, i.e. $E^{\#}_{13} = \sqrt{E^2_{13'} + E^2_{23'}}$, hence resulting into a truly frame invariant quantity. Additionally, the axial strains are constrained by the incompressibility condition $E_{11} + E_{22} + E_{33} = 0$.

The generalized Kirchhoff stress tensor $\mathbf{T}$, work-conjugate of the material logarithmic strain tensor, see [30], is $-p$ is an initially undetermined pressure-like Lagrange multiplier to be determined from boundary conditions

$$\mathbf{T} = \frac{\partial \mathcal{W}(\mathbf{E}, \mathbf{a}_3)}{\partial \mathbf{E}} + p \tag{26}$$

$$= \sum_{i=1}^{3} \omega'_{ii}(E_{ii})\mathbf{a}_i \otimes \mathbf{a}_i + \sum_{j=1}^{2} \omega'_{13}\big(E^{\#}_{13}\big)\frac{E_{j3}}{E^{\#}_{13}}\big(\mathbf{a}_j \otimes \mathbf{a}_3 + \mathbf{a}_3 \otimes \mathbf{a}_j\big) + p \tag{27}$$

where we have used that

$$\frac{dE_{ij}}{d\mathbf{E}} = \mathbf{a}_i \otimes \mathbf{a}_j, \quad i, j = 1, 2, 3 \tag{28}$$

with the symbol $\otimes$ representing the usual dyadic product, and that

$$\frac{\partial E^{\#}_{13}}{\partial E_{j3}} = \frac{E_{j3}}{E^{\#}_{13}}, \quad j = 1, 2 \tag{29}$$

and we have already taken into consideration the corresponding symmetries (formally, and only for differentiation purposes, note that $2\omega_{13}(E^{\#}_{13}) = \omega_{13}(E^{\#}_{13}) + \omega_{13}(E^{\#}_{31})$ with $E^{\#}_{31} = \sqrt{E^2_{31} + E^2_{32}} \equiv E^{\#}_{13}$).

As previously mentioned, three complete curves in different directions (with five independent branches) are sufficient to determine the contributions $\omega_{11}$, $\omega_{33}$ and $\omega_{13}$ (note that $\omega_{13}$ is defined for $E^{\#}_{13} \geq 0$ only). Assuming that the stress-strain behavior can be obtained from the load-displacement curves, the contributions are determined.

As usual in transversely isotropic material models, we will consider that the preferred direction $\mathbf{a}_3$ represents the stiffer direction. For the data shown in Fig. 2, this direction corresponds to the test at 0°. The test at 90°is then performed about an isotropic direction in the model. Using these two tests the contributions $\omega_{11}$ and $\omega_{33}$ can be determined. The remaining contribution $\omega_{13}$ is determined using the data from the test at 45°.

*4.2. Determination of $\omega'_{11}(E_{11})$ and $\omega'_{33}(E_{33})$ from $\sigma^{(1)}_{11}(E_{11})$ and $\sigma^{(3)}_{33}(E_{33})$*

The following algorithmic iterative procedure exactly solves (from a numerical viewpoint) Equations (63)–(65) of Ref. [27], which are the governing equations of two uniaxial tests, one in the isotropic direction $\mathbf{a}_1$ (hence the superscript (1) in $\sigma^{(1)}_{11}(E_{11})$) and the other one in the anisotropic direction $\mathbf{a}_3$ (hence the superscript (3) in $\sigma^{(3)}_{33}(E_{33})$). Note that, since the loading path is along preferred directions in both tests and the material is considered purely incompressible during the strain energy determination procedure, the generalized Kirchhoff stress tensor $\mathbf{T}$ in Eq. (27) is coincident to both the Kirchhoff stress tensor $\tau$ and the Cauchy stress tensor $\sigma = J^{-1}\tau$ [30], where $J$=1 is the volume ratio (i.e. $\ln J = tr\mathbf{E} = 0$). The Lagrange multiplier $p$ in Eq. (27) is immediately obtained from the traction-free boundary conditions in the transverse directions in the respective tests. We rephrase herein the governing equations for the reader convenience—since the test directions are principal directions we use just one index $(ii) \to (i)$ for strain and stress components

$$\sigma^{(1)}_1(E_1) = \frac{d\omega_{11}(E_1)}{dE_1} - \frac{d\omega_{11}(E_2)}{dE_2}\bigg|_{E^{(1)}_2(E_1)} \tag{30}$$

$$\frac{d\omega_{11}(E_2)}{dE_2}\bigg|_{E^{(1)}_2(E_1)} = \frac{d\omega_{33}(E_3)}{dE_3}\bigg|_{E^{(1)}_3(E_1)} \tag{31}$$

and

$$\sigma^{(3)}_3(E_3) = \frac{d\omega_{33}(E_3)}{dE_3} - \frac{d\omega_{11}(E_1)}{dE_1}\bigg|_{-E_3/2} \tag{32}$$

where $E^{(1)}_2(E_1)$ (or $E^{(1)}_3(E_1)$) represents the transverse strains in axis 2 (or axis 3) during the test about the axis 1. Note that $E_1 + E^{(1)}_2 + E^{(1)}_3 = 0$ by incompressibility. For the same reason, during the test about the anisotropic axis, we obtain $E^{(3)}_1(E_3) = E^{(3)}_2(E_3) = -E_3/2$, see Eq. (32). The difference between the present procedure and the procedure detailed in Table 3 of Ref. [27] is that we do not need to assume the shape of the transverse-to-axial strain relation (by Poisson's effect in test 1) $E^{(1)}_2(E_1)$. This is possible thanks to the additional use of a continuous spline interpolation of that transverse strain function, which was considered linear in Ref. [27]. Once a solution has been obtained, the model exactly replicates (i.e. to machine precision if desired) the in-axial behavior of the transversely isotropic material about its preferred directions. The following algorithm is equivalent to the improvement presented for the orthotropic case in [32].

1. Spline-based smooth continuous functions $\sigma^{(1)}_1(E_1)$ and $\sigma^{(3)}_3(E_3)$ are obtained from the interpolation of the tension-compression experimental data points (experimental noise should be previously removed from data). These spline-based functions, say $f_i(x)$, have to satisfy the requirements $f_i(0) = 0$. The slopes at the origin of these curves are, respectively $Y_1$ and $Y_3$ (Young's moduli).
2. Take the linearized relation for transverse strains in the isotropic plane as $E^{(1)}_2(E_1) = -\nu_{12}E_1$, associated to the corresponding infinitesimal behavior, just to initialize the iterative procedure (iteration $k$=0). The initial Poisson ratio $\nu_{12}$ is given from the linear theory as in [21]

$$\nu_{12} = 1 - \nu_{13} = 1 - \nu_{31}\frac{Y_1}{Y_3} = 1 - \frac{Y_1}{2Y_3} \tag{33}$$

where

$$Y_1 = \frac{d\sigma^{(1)}_1(E_1)}{dE_1}\bigg|_{E_1=0} \quad \text{and} \quad Y_3 = \frac{d\sigma^{(3)}_3(E_3)}{dE_3}\bigg|_{E_3=0} \tag{34}$$

3. Compute the initial ($k$=0) spline-based functions $\omega'_{11}(E_1)$ and $\omega'_{33}(E_3)$ associated to the initial transverse distribution $E^{(1)}_2(E_1)$ solving numerically Eqs. (30)–(32), i.e. following steps 3 and 4 in Table 3 of Ref. [27].
4. Update the first derivative function of $E^{(1)}_2(E_1)$ at iteration $k+1$ through

$$\frac{dE^{(1)}_2(E_1)}{dE_1}\bigg|_{k+1} = -\frac{\omega''_3(E^{(1)}_3(E_1))}{\omega''_1(E^{(1)}_2(E_1)) + \omega''_3(E^{(1)}_3(E_1))}\bigg|_k \tag{35}$$

which is obtained after differentiating Eq. (31) and considering the incompressibility constraint $E_1 + E^{(1)}_2(E_1) + E^{(1)}_3(E_1) = 0$. Remarkably, Eq. (35) is the non-linear counterpart of the small strain Poisson's ratio $\nu_{12}$ expressed in terms of the deviatoric moduli $\mu_2 \equiv \mu_1$ and $\mu_3$—cf. the general orthotropic Relation (140) in Ref. [29].
5. Build the piecewise cubic spline $(E_1, dE^{(1)}_2(E_1)/dE_1)_{k+1}$. Note that for this function, say $g(x)$, the requirement $g(0) = 0$ does not have to be enforced.
6. Integrate the first-derivative functions of step 5 and then build the updated spline $E^{(1)}_2(E_1)$ at iteration $k+1$. At this step, consider the (integration) requirement $E^{(1)}_2(0) = 0$.
7. Compute the updated spline-based functions $\omega'_{11}(E_1)$ and $\omega'_{33}(E_3)$ solving numerically Eqs. (30)–(32), i.e. following steps 3 and 4 in Table 3 of Ref. [27].
8. Quantify the associated relative error for the transverse strains $E^{(1)}_2(E_1)$ between iterations $k$ and $k+1$. Exit if *error* ≤ *tolerance*. Take $k \leftarrow k+1$ and go to step 4 if *error* > *tolerance*.

In contrast to most hyperelasticity model determination procedures, we remark that we do not perform a least-squares optimization of our model to fit the experimental data. We apply an iterative non-linear solution method that finds the terms $\omega'_{11}(E_1)$ and $\omega'_{33}(E_3)$ that exactly replicate the prescribed experimental data. Furthermore, this algorithm removes any need to prescribe initial values for the iterative procedure; the required values to initialize the procedure are contained in the experimental data of Step 1. This self-contained algorithm is capable of converging to machine precision tolerances (*tolerance* = $10^{-14}$) although the predictions were observed, in practice, undistinguishable for *tolerance* = $10^{-3}$, which is a tolerance we typically enforce.

*4.3. Determination of $\omega'_{13}$ from a tensile uniaxial test at 45°*

In Ref. [27] we explained how the first derivative function $\omega'_{13}(E^{\#}_{13}) \equiv \omega'_{13}(E_{13})$ can be determined from two different shear tests, namely a pure shear test (Section 3.2.1 in [27]) and a simple shear test (Section 3.2.2 of the same Reference). We explain herein the procedure to determine the stored energy shear term from stress-strain data obtained from a uniaxial test performed at 45° with respect to the anisotropic direction $\mathbf{a}_3$. The shear term $\omega'_{13}(E^{\#}_{13})$ presents only one (positive) branch, so only the tension branch of this uniaxial test is needed; recall that both tension and compression branches of $\sigma^{(1)}_{11}(E_{11})$ and $\sigma^{(3)}_{33}(E_{33})$ are required for the determination of $\omega'_{11}(E_{11})$ and $\omega'_{33}(E_{33})$ [26].

We denote the test reference frame as $X = \{\mathbf{e}_1, \mathbf{e}_2, \mathbf{e}_3\}$ and the preferred material axes as $X_{pr} = \{\mathbf{a}_1, \mathbf{a}_2, \mathbf{a}_3\}$. We consider $\mathbf{a}_2 \equiv \mathbf{e}_2$ and that the anisotropic direction $\mathbf{a}_3$ is counter-clockwise oriented at 45° with respect to $\mathbf{e}_3$, as shown in Fig. 8. In the case herein considered, the uniaxial test is performed about direction $\mathbf{e}_1$. We assume a uniform deformation state over the *differential element* of Fig. 8. The faces with normals $\mathbf{e}_2$ and $\mathbf{e}_3$ are ideally traction-free, so we will impose the boundary conditions $[\sigma_{22}]_X = [\sigma_{33}]_X = 0$ where by $[\cdot]_X$ we mean that we used the system of representation X.

We prevent herein any shear deformations in the test frame (this will be assessed below) so that no angular distortion is present in the element under study. Hence, directions $\{\mathbf{e}_1, \mathbf{e}_2, \mathbf{e}_3\}$ are coincident with the (Lagrangian and Eulerian) principal strain directions. The logarithmic strain tensor $\mathbf{E}$ expressed in the system of reference $X$ reads—we represent only components in the plane $\{\mathbf{e}_1, \mathbf{e}_3\}$

$$[\mathbf{E}]_X = \begin{bmatrix} E_{11} & E_{13} \\ E_{13} & E_{33} \end{bmatrix}_X = \begin{bmatrix} E_1 & 0 \\ 0 & E_3 \end{bmatrix} = \begin{bmatrix} \ln\lambda_1 & 0 \\ 0 & \ln\lambda_3 \end{bmatrix} \tag{36}$$

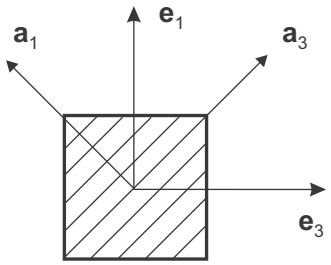


**Fig. 8.** Test axes $X = \{\mathbf{e}_1, \mathbf{e}_3\}$ and preferred material axes $X_{pr} = \{\mathbf{a}_1, \mathbf{a}_3\}$ for the uniaxial tensile test at 45°. The loading direction is $\mathbf{e}_1$.

where $\lambda_1$ and $\lambda_3$ are the principal stretches in directions $\mathbf{e}_1$ and $\mathbf{e}_3$, respectively. We assume perfect incompressibility, so the volume ratio is $J = \lambda_1\lambda_2\lambda_3 = 1$ and the remaining principal strain (not shown in the matrix operations for brevity) is $E_2 = \ln\lambda_2 = -E_1 - E_3$. The in-plane components of the tensor $\mathbf{E}$ in $X_{pr}$ are —note that $[E_{23}]_{X_{pr}} = 0$ so $E^{\#}_{13} = |E_{13}| = [E_{13}]_{X_{pr}} > 0$

$$[\mathbf{E}]_{X_{pr}} = \begin{bmatrix} E_{11} & E_{13} \\ E_{13} & E_{33} \end{bmatrix}_{X_{pr}} = \frac{1}{2}\begin{bmatrix} E_1 + E_3 & E_1 - E_3 \\ E_1 - E_3 & E_1 + E_3 \end{bmatrix} \tag{37}$$

where we note that $[E_{33}]_{X_{pr}} = [E_{11}]_{X_{pr}}$.

The preferred in-plane components of the generalized Kirchhoff stress tensor $\mathbf{T}$ of Eq. (27) are

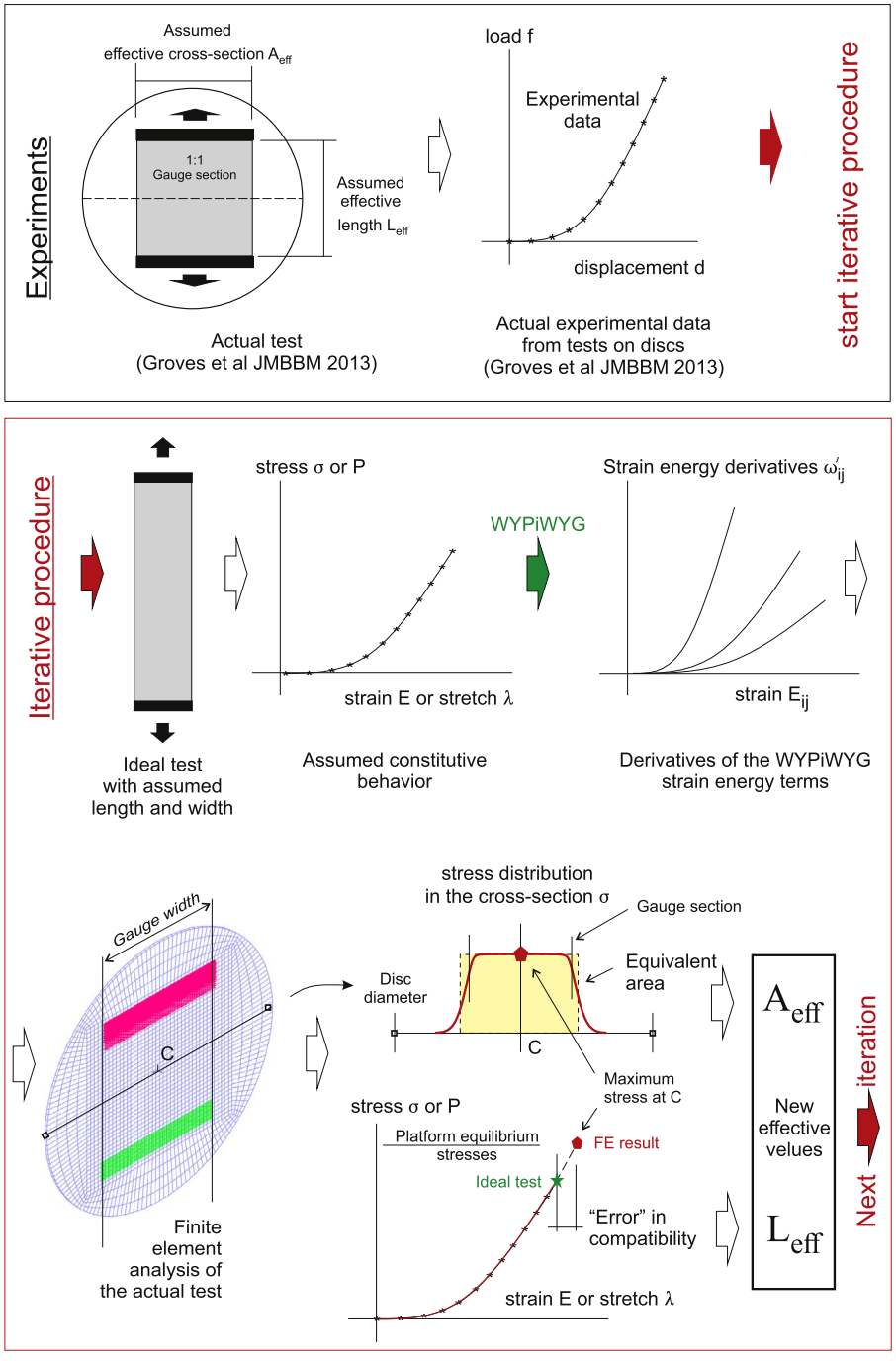


**Fig. 9.** Iterative procedure, departing from the experimental data of Groves et al. [16], to obtain the final stress-strain curves and the corresponding stored energy function terms. In practice, only one iteration was needed.

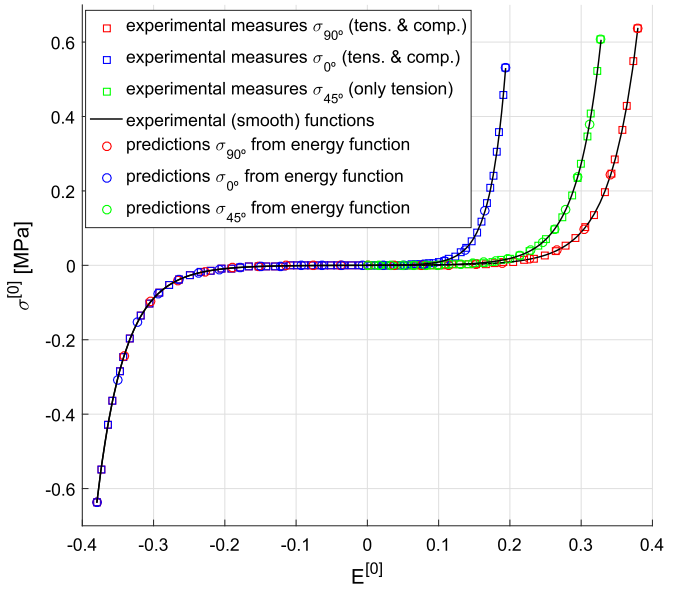


**Fig. 10.** Experimentally-derived uniaxial stress-strain curves for tests at 0°, 45° and 90° in the initial case [0]. Stresses are obtained from measured loads using $A_{eff}^{[0]}$ and strains are obtained from measured displacements using $L_{eff}^{[0]}$. Uniaxial compression stress-strain data at 0° and 90° are both assumed to be matrix-dominated and made equal to minus the tensile stress-strain data at 90°. Predictions for the three tests from the computed strain energy function (not shown at this initial stage) are also shown.

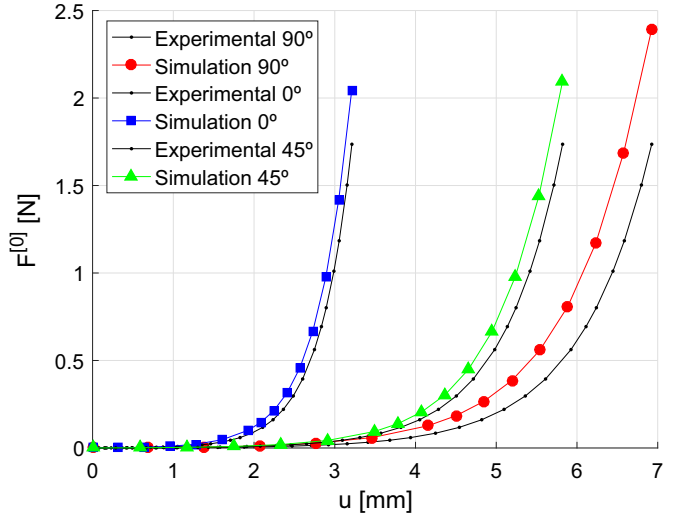


**Fig. 11.** Experimental and computed load-displacement curves at 0°, 45° and 90° in the initial case [0]. Finite element simulations are performed using the strain energy function associated to $A_{eff}^{[0]}$ and $L_{eff}^{[0]}$.

$$[\mathbf{T}]_{X_{pr}} = \begin{bmatrix} T_{11} & T_{13} \\ T_{13} & T_{33} \end{bmatrix}_{X_{pr}} \tag{38}$$

$$= \begin{bmatrix} \omega'_{11}(E_{11}) + p & \omega'_{13}(E_{13}) \\ \omega'_{13}(E_{13}) & \omega'_{33}(E_{33}) + p \end{bmatrix}_{X_{pr}} = \left[\frac{d\mathcal{W}}{d\mathbf{E}} + p\mathbf{I}\right]_{X_{pr}} \tag{39}$$

where we note that $[T_{33}]_{X_{pr}} > [T_{11}]_{X_{pr}}$, in general. We can determine $p$ from the stress boundary condition $\sigma_{22} = 0 = T_{22}$, which gives

$$0 = \omega'_{11}(E_{22}) + p = \omega'_{11}(E_2) + p \tag{40}$$

$$\Longrightarrow \quad p = -\omega'_{11}(-E_1 - E_3) \tag{41}$$

where we have used the fact that $[E_{22}]_{X_{pr}} = E_2 = -E_1 - E_3$. Hence, using Eqs. (39)–(41), the in-plane components of $\mathbf{T}$ in preferred material directions, expressed in terms of the principal strains $E_1$ and $E_3$, are

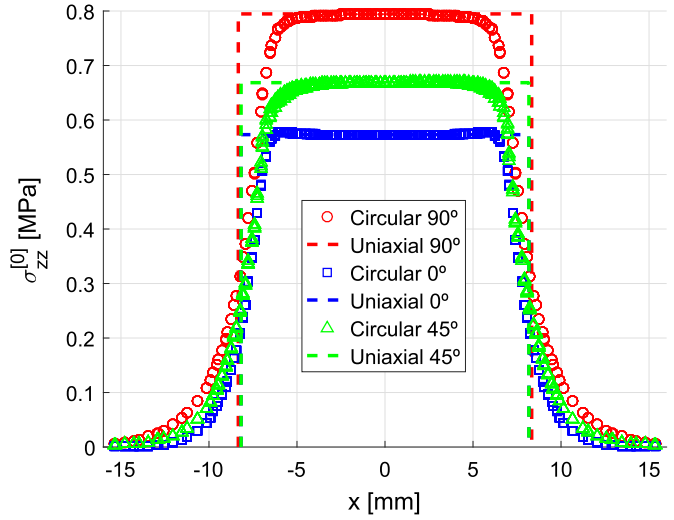


**Fig. 12.** Distributions of axial stresses in loading direction (global axis Z) over the undeformed central section width (global axis X) for the three tensile tests at 0°, 45° and 90° in the initial case [0]. The undeformed effective widths $w_{eff}^{[0]} \approx 16.5$mm of the respective equivalent ideal uniaxial specimens that give the same force resultants are illustrated (distance between respective vertical lines). Maximum load (last step) is considered for each test.

$$[T_{11}]_{X_{pr}} = \omega'_{11}\left(\frac{E_1 + E_3}{2}\right) - \omega'_{11}(-E_1 - E_3) \tag{42}$$

$$[T_{33}]_{X_{pr}} = \omega'_{33}\left(\frac{E_1 + E_3}{2}\right) - \omega'_{11}(-E_1 - E_3) \tag{43}$$

$$[T_{13}]_{X_{pr}} = \omega'_{13}\left(\frac{E_1 - E_3}{2}\right) \tag{44}$$

Once the expression of the tensor $\mathbf{T}$ is known in the preferred material axes $X_{pr}$, it has to be represented in the test axes $X$ in order to be able to apply the remaining loading and boundary conditions, i.e.

$$[\mathbf{T}]_X = \frac{1}{2}\begin{bmatrix} [T_{11}]_{X_{pr}} + 2[T_{13}]_{X_{pr}} + [T_{33}]_{X_{pr}} & [T_{33}]_{X_{pr}} - [T_{11}]_{X_{pr}} \\ [T_{33}]_{X_{pr}} - [T_{11}]_{X_{pr}} & [T_{11}]_{X_{pr}} - 2[T_{13}]_{X_{pr}} + [T_{33}]_{X_{pr}} \end{bmatrix} \tag{45}$$

We observe that a shear stress component $[T_{13}]_X = \frac{1}{2}([T_{33}]_{X_{pr}} - [T_{11}]_{X_{pr}}) > 0$ is present in the test axes as a reaction to the imposed angular distortion restriction. We assume that this reaction stress is carried by the grips in rectangular specimens (and also by the extra material for the case of circular specimens). We will confirm this assumption in the finite element analysis below. In case this condition were not holding, a further (more complex) iterative procedure would need to be established. The specific value of $[T_{13}]_X$ is not needed in the following lines. We also note that $\mathbf{T}$ and $\mathbf{E}$ are not coaxial (compare Eqs. (36) and (45)), so $\{\mathbf{e}_1, \mathbf{e}_3\}$ are not principal stress directions, in general. This lack of coaxiality can be interpreted as a Cosserat-alike moment which tends to produce local rotations, see [29] in the context of viscoelasticity and [36] in the context of plasticity.

Finally, the diagonal components of $\mathbf{T}$, expressed in the Lagrangian strain basis $X$, are coincident with the diagonal components of the rotated Kirchhoff stress tensor $\bar{\tau}$, expressed in the same basis, see [30]. In this case, the Lagrangian and Eulerian strain basis are coincident, and $J$=1, so $\bar{\tau} = \tau = \mathbf{J}\sigma = \sigma$, whereupon the axial (diagonal) components of the Cauchy stress tensor in the test axes are

$$[\sigma_{11}]_X = [T_{11}]_X = \frac{1}{2}([T_{11}]_{X_{pr}} + 2[T_{13}]_{X_{pr}} + [T_{33}]_{X_{pr}}) \tag{46}$$

$$[\sigma_{33}]_X = [T_{33}]_X = \frac{1}{2}([T_{11}]_{X_{pr}} - 2[T_{13}]_{X_{pr}} + [T_{33}]_{X_{pr}}) \tag{47}$$

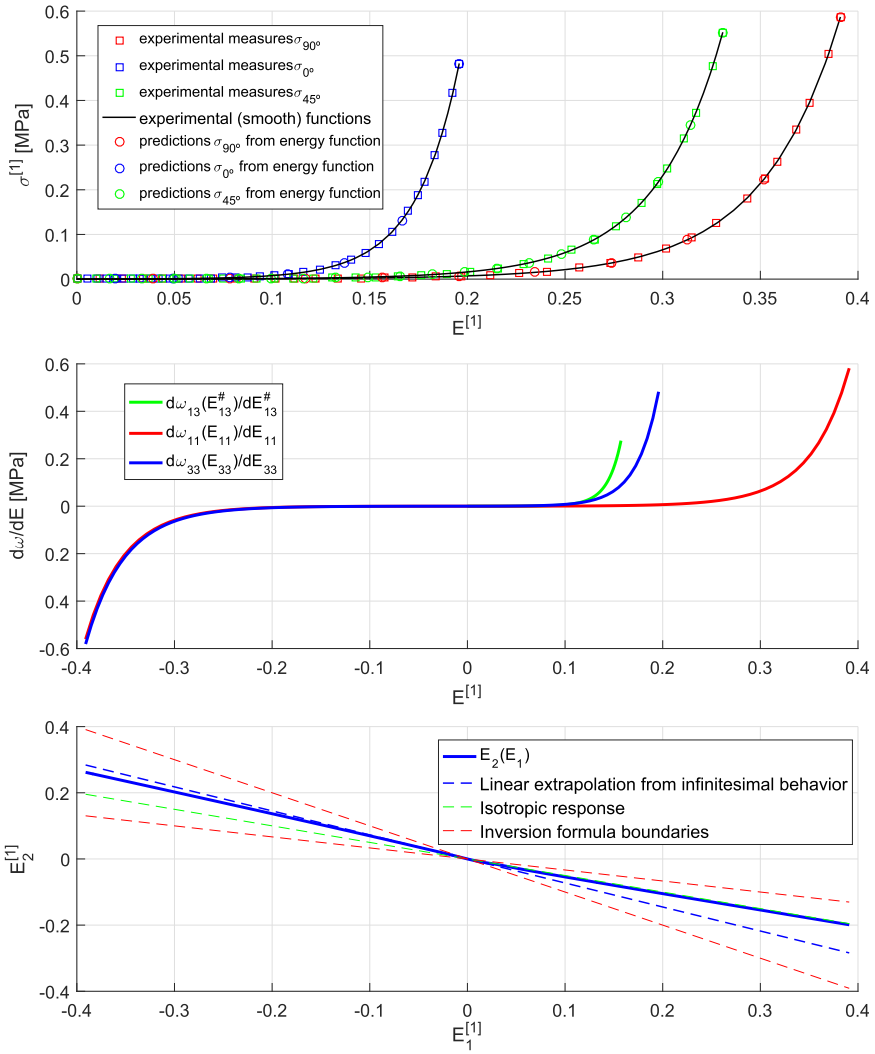


**Fig. 13.** Top (a): Experimentally-derived and predicted uniaxial stress-strain curves for tests at 0°, 45° and 90° at stage [1]. Experimental stresses are obtained from measured loads using $A^{[1]}_{eff}$ and experimental strains are obtained from measured displacements using $L^{[1]}_{eff}$. Uniaxial compression stress-strain data at 0° and 90° are both assumed to be matrix-dominated and made equal to minus the tensile stress-strain data at 90° (not shown). Center (b): Computed WYPiWYG strain energy terms from experimental distributions. Bottom (c): Non-linear transverse strains (by Poisson's effect) in material direction 2 during the uniaxial test in material direction 1 (i.e. uniaxial test at 90°) computed as a part of the iterative procedure of Section 4.

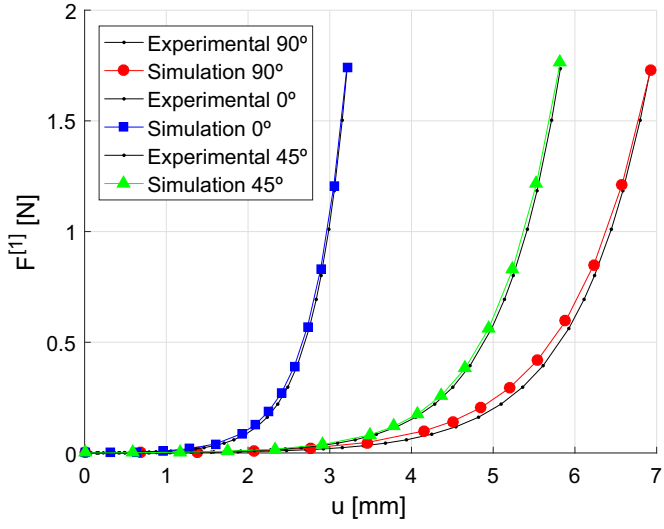


**Fig. 14.** Experimental and computed load-displacement curves at 0°, 45° and 90° at stage [1]. Finite element simulations are performed using the strain energy function associated to $A^{[1]}_{eff}$ and $L^{[1]}_{eff}$, see Fig. 13*b*.

From experimental measurements we know the curve $[\sigma_{11}]_X$ as a function of $[E_{11}]_X \equiv E_1 = \ln\lambda_1$, which we represent as $\sigma_{45°}(E_1)$. We also know the boundary condition $[\sigma_{33}]_X = 0$. Then, adding Eqs. (46) and (47), and substracting Eq. (47) from Eq. (46), we arrive respectively at the following non-linear equations

$$\sigma_{45°}(E_1) = \omega'_{11}\left(\frac{E_1+E_3}{2}\right) + \omega'_{33}\left(\frac{E_1+E_3}{2}\right) - 2\omega'_{11}(-E_1-E_3) \tag{48}$$

$$\sigma_{45°}(E_1) = 2\omega'_{13}\left(\frac{E_1-E_3}{2}\right) \tag{49}$$

where we have already substituted Eqs. (42)–(44). Note that $E_1 = [E_{11}]_X$ (known) and $E_3 = [E_{33}]_X$ (unknown) are principal strains and $\sigma_{45°}:=[\sigma_{11}]_X$ (known for a given $E_1$ from the experiment). Then Eq. (48) is a non-linear equation from which we can obtain the transverse strain $E_3 < 0$ for each input value $E_1 > 0$. Note that we need the spline-based functions $\omega'_{11}(E_{11})$ and $\omega'_{33}(E_{33})$, computed as described in the previous subsection. Once $E_1$ and $E_3(E_1)$ are known, Eq. (49) gives the associated value of $\omega'_{13}(E^{\#}_{13})$, with $E^{\#}_{13} = \frac{1}{2}(E_1 - E_3)$.

The procedure to obtain the spline-based function $\omega'_{13}(E^{\#}_{13})$ is summarized as follows—we use the tilde decoration for experimental data points and associated values

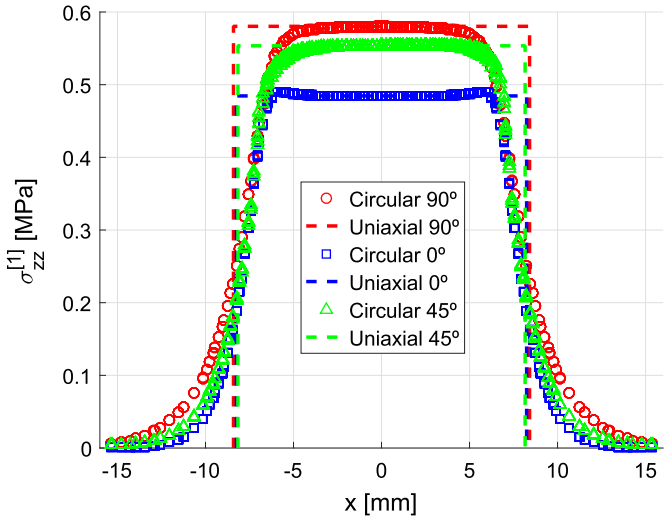


**Fig. 15.** Distributions of axial stresses in loading direction (global axis Z) over the undeformed central section width (global axis X) for the three tensile tests at 0°, 45° and 90° at stage [1]. The undeformed effective widths $w_{eff}^{[1]} \approx 16.5$mm of the respective equivalent ideal uniaxial specimens that give the same force resultants are illustrated (distance between respective vertical lines). Maximum load (last step) is considered for each test.

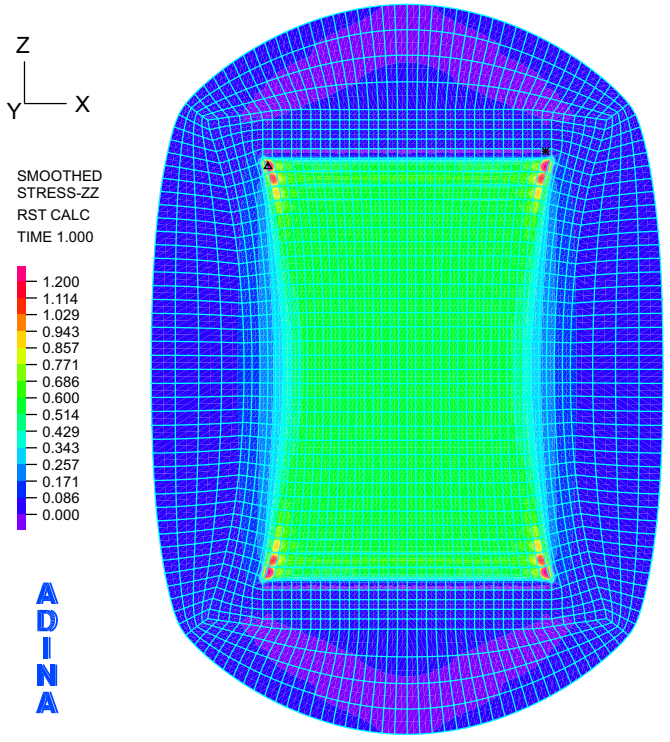


**Fig. 16.** Deformed configuration of the disc and Cauchy stress field $\sigma_{zz}$ for the tensile test at 90° (i.e. about material direction 1) under maximum load ($u_z = 6.93$mm).

$$\left.\begin{matrix}\text{Experim.}\\ \text{data pairs:}\\ \{\widetilde{\mathbf{E}}_1,\ \widetilde{\sigma}_{45^\circ}\}\end{matrix}\right\} \xrightarrow[\text{spline}]{\text{Smooth}} \sigma_{45^\circ}(E_1) \xrightarrow[\text{at each } \widetilde{E}_1]{\text{Eq.(48)}} \widetilde{E}_3(\widetilde{E}_1) \xrightarrow[\text{at each } \widetilde{E}_1]{\text{Eq.(37)}}$$

$$\xrightarrow[\text{at each } \widetilde{E}_1]{\text{Eq.(37)}} \widetilde{E}_{13}^{\#} = \frac{\widetilde{E}_1 - \widetilde{E}_3(\widetilde{E}_1)}{2} \xrightarrow[\text{at each } \widetilde{E}_1]{\text{Eq.(49)}} \widetilde{\omega}'_{13}(\widetilde{E}_{13}^{\#}) = \frac{\widetilde{\sigma}_{45^\circ}(\widetilde{E}_1)}{2} \xrightarrow[\text{interp.}]{\text{Spline}} \omega'_{13}(E_{13}^{\#})$$

In order to gain efficiency in finite element calculations whenever the spline-based model is addressed, the piecewise spline function $\omega'_{13}(E_{13}^{\#})$ should be re-built using uniform intervals before storing its coefficients in memory.

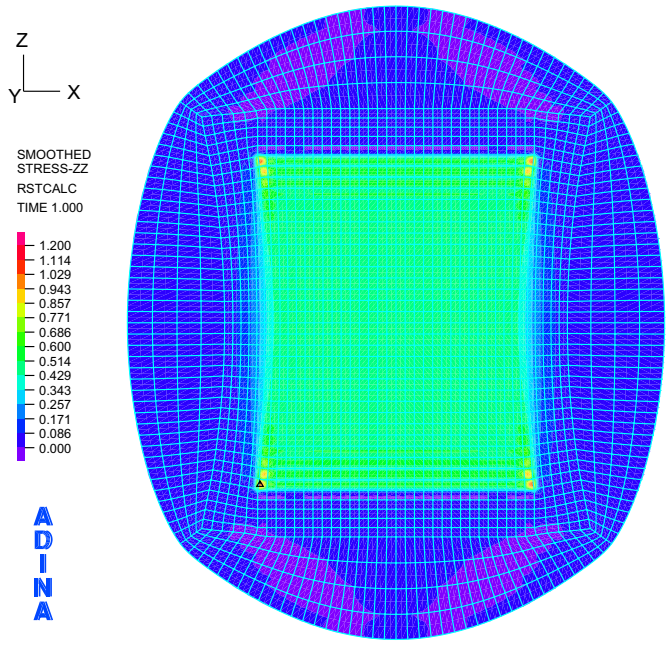


**Fig. 17.** Deformed configuration of the disc and Cauchy stress field $\sigma_{zz}$ for the tensile test at 0° (i.e. about material direction 3) under maximum load ($u_z = 3.21$mm).

## 5. Stress-strain and load-displacement predictions through FEM experiments

As we have just explained, the WYPiWYG transversely isotropic hyperelastic model requires three *stress-strain* curves in order to be completely defined. However, the experimental data described in Section 2 are *load-displacement* curves. In this section the relationships between the load-displacement curves and the required stress-strain ones are examined. The relationship is based on the concept of an effective area and effective length (basic concepts borrowed from Strength of Materials), both resulting from the fact that the tested specimens are not ideal uniaxial specimens. Finite element simulations of the circular specimens were used to identify both magnitudes. Then, equivalent uniaxial stress-strain curves are predicted based on physical reasoning and the values are refined using an additional simulation. Finally, we reproduce the load-displacement curves obtained experimentally, which is the main purpose of the procedure. Interestingly, the non-linear load-displacement behavior allows for the prediction of the stress-strain response just attending to the uniaxial response assumption previously discussed. This simplifying hypothesis has been proved to be valid, as we show next.

The characterization of circular specimen tests for isotropic materials was described in Section 3. The next step is to extend the hypothesis to the transversely isotropic behavior. The three tests by Groves et al. at 0°, 45°, and 90° will be referred to as longitudinal direction, diagonal direction and transverse direction, respectively.

### 5.1. Methodology and results

Based on the results obtained using the Ogden model for the loads on the disc, the objective is to identify equivalent areas and equivalent lengths for the skin specimen under study which allows us to replicate the load displacement responses obtained by [16]. This identification was achieved through finite element simulations of the circular specimen. The same finite element model from Section 3 is used in order to obtain the skin strain energy density using the WYPiWYG transversely isotropic model described in Section 4.

The procedure that we have conducted consists of the following steps, see Fig. 9. First, for iteration [0], an initial reference cross-

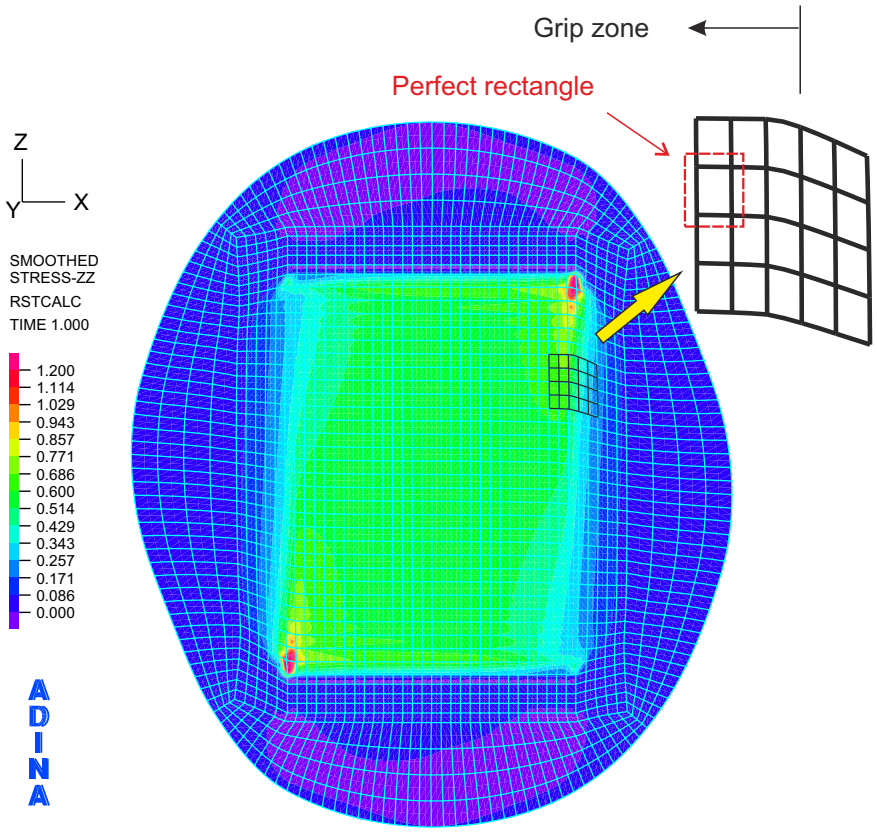


**Fig. 18.** Deformed configuration of the disc and Cauchy stress field $\sigma_{zz}$ for the tensile test at 45° (i.e. about direction $\mathbf{e}_1$ in Fig. 8) under maximum load ($u_z = 5.82$mm).

sectional area $A_{eff}^{[0]} = w_{eff}^{[0]} \times h = 15 \times 0.265\text{mm}^2$ was assumed for the three tensile tests considering the clamps width (15 mm) and the thickness of the sample (0.256mm). This area permits to estimate the assumed *uniaxial* first Piola-Kirchhoff (nominal) stresses from the respective measured loads $F$ (ordinates in Fig. 2) just as $P^{[0]} = F/A_{eff}^{[0]}$. Additionally, an initial reference length $L_{eff}^{[0]} = 15$mm was assumed for the three tensile tests considering the distance between clamps. This length permits to estimate the assumed *uniaxial* stretches from the respective measured displacements $u$ (abscissae in Fig. 2) just as $\lambda^{[0]} = (L_{eff}^{[0]} + u)/L_{eff}^{[0]}$. The resulting assumed *uniaxial* Cauchy stresses and logarithmic strains for the initial case are obtained for the respective tensile test by means of $\sigma^{[0]} = P^{[0]}\lambda^{[0]}$ and $E^{[0]} = \ln\lambda^{[0]}$. This way, after smoothing these data in order to remove experimental noise, we obtain the three uniaxial stress-strain curves needed as input data for the procedures described in Section 4, i.e. $\sigma_1^{(1)}(E_1)$ (transversely isotropic direction at 90°), $\sigma_3^{(3)}(E_3)$ (longitudinal direction at 0°) and $\sigma_{45°}(E_1)$ (diagonal direction at 45°). The strain energy first-derivative functions $\omega'_{11}(E_{11})$, $\omega'_{33}(E_{33})$ and $\omega'_{13}(E_{13}^{\#})$ are then determined as explained in the previous section. We show in Fig. 10 the three uniaxial stress-strain distributions with their corresponding smoothed continuous curves. In this figure we can see the compression responses that we have assumed for the uniaxial curves about preferred directions, i.e. at 0° and 90° (no assumption is needed at 45°). We also show some stress-strain points predicted from the strain energy being computed (which is not shown at this initial stage). As expected in WYPiWYG hyperelasticity procedures, we can observe in this figure the perfect (exact, in practice) agreement between the *gotten* predictions and the *prescribed* stress-strain data. However, note that this fact is inherent to WYPiWYG procedures, but it does not mean that the strain energy function obtained at this initial stage is the sought solution that yields the actual load-displacement curve in the real non-homogeneous test. If the next simulations do not reproduce the load-displacement curves, it will mean that the initial selected values of $A_{eff}$ and/or $L_{eff}$ (from which the prescribed stress-strain data have been obtained) are not accurate to represent such nonhomogeneous problem, so additional iterations will be needed in order to obtain more appropriate values for those geometrical parameters.

At this point the material model is completely defined and the simulations can be performed. We have employed a user material subroutine in the general-purpose finite element program ADINA in order to compute the stresses and tangent moduli from a given deformation gradient at each integration point and iteration during the nonlinear computations. We show in Fig. 11 the load-displacement curves obtained from the respective finite element simulations over the disc. We can see that the predictions separate from the experimental curves at this initial stage. In Fig. 12 we show the distribution about the central section width of axial stresses in the loading direction for each case under maximum load. We observe that the stress distributions in the central region of the specimen are fairly flat and resemble those of typical uniaxial tests, which reinforce the underlying hypothesis of equivalent uniaxial responses over the three directions (i.e. lateral restriction effects are negligible in all cases, recall the simplified analysis of Section 3.1).

We can obtain some feedback from Fig. 12 in order to modify both the initial effective area and length for each case. First, we observe that the computed stresses in the flat areas are $\sigma_{0°} \approx 0.57$MPa, $\sigma_{45°} \approx 0.67$MPa and $\sigma_{90°} \approx 0.79$MPa. However, the stresses for maximum load shown in Fig. 10 are $\sigma_{0°}^{max} \approx 0.53$MPa, $\sigma_{45°}^{max} \approx 0.61$MPa and $\sigma_{90°}^{max} \approx 0.64$MPa. These differences between computed stresses and prescribed stresses mean that the axial strains in the central regions of the respective disc simulations have been higher, so the effective length must be modified accordingly at each test in order to prescribe more accurate axial strains, see [48] in the context of arteries. Through the intersections of the computed values $\sigma_{0°}$, $\sigma_{45°}$ and $\sigma_{90°}$ and the respective curves in Fig. 10, we obtain the following effective lengths for each test

$$L_{eff}^{[1]}|_{0^\circ} = 0.99 \times L_{eff}^{[0]}, \quad L_{eff}^{[1]}|_{45^\circ} = 0.99 \times L_{eff}^{[0]}, \quad L_{eff}^{[1]}|_{90^\circ} = 0.965 \times L_{eff}^{[0]} \tag{50}$$

which will be used to define the prescribed stretches $\lambda^{[1]} = (L_{eff}^{[1]} + u)/L_{eff}^{[1]}$ (i.e. the $x$–axis of the stress-strain curve) for the next strain energy determination procedure. Note that we are assuming for now the equality between the stretch and that of the uniaxial ideal experiment, an assumption that follows from the findings in Ref. [48]; subsequently the effective length will be corrected during the iterative procedure. On the other hand, we also represent in Fig. 12 the effective *uniaxial* width for each case, i.e. the width that gives equivalence of axial force between the computed non-uniform distribution and an assumed uniform distribution over the effective width for each case, see Eq. (22). The effective widths result very similar in value for the three cases, so we take the same value for the reference effective cross-sectional areas over the three directions and, of course, for all deformation values—note that we preserve the value of the sample thickness at iteration [1], i.e. $A_{eff}^{[1]} = w_{eff}^{[1]} \times h$

$$A_{eff}^{[1]}|_{0^\circ} = A_{eff}^{[1]}|_{45^\circ} = A_{eff}^{[1]}|_{90^\circ} = 1.1 \times A_{eff}^{[0]} \tag{51}$$

which will be used to define the prescribed nominal stresses $P^{[1]} = F/A_{eff}^{[1]}$ for the next strain energy determination procedure.

We show in Fig. 13*a* the resulting uniaxial stress-strain distributions computed using the new values $L_{eff}^{[1]}$ and $A_{eff}^{[1]}$ for each test. The corresponding strain energy function terms obtained upon the application of the procedures explained in Section 4 are shown in Fig. 13*b*. Again, exact predictions from the (new) strain energy function being calculated are obtained, see Fig. 13*a*, which are possible due to the consideration of a nonlinear transverse-to-axial strain relation $E_2^{(1)}(E_1)$ being computed as a part of the procedure, as we explained in Section 4, see Fig. 13*c*. Interestingly, in this last figure we can see that the transverse deformation for tensile loading in the test at 90° is nearly isotropic, i.e. $E_2^{(1)}(E_1 > 0) \simeq -\frac{1}{2}E_1$, which is a consequence of the fact that we have assumed that fibers (oriented about material direction 3, within the transverse plane during the test at 90°) do not work in compression. In other words, we have prescribed matrix-dominated responses during compressive behavior, see Figs. 13*a* and *b*. On the contrary, the transverse deformation for compressive loading in the test at 90° is no longer isotropic, i.e. $E_2^{(1)}(E_1 < 0) \neq -\frac{1}{2}E_1$ because the fibers (within the transverse plane during the test at 90°) would be in extension in this case and increase the stiffness about material direction 3, see Figs. 13*a* and *b*. Clearly, WYPiWYG procedures allows us both to prescribe stress-strain data and to interpret results using engineering judgement.

The material model at this new iteration [1] is completely defined and the same simulations over the disc can be performed again. We show in Fig. 14 the new load-displacement curves obtained from the respective finite element simulations. We can see that an excellent agreement with the experimental curves is achieved in this case. Note that the agreement is slightly weaker for 90° (the softer direction) which explanation comes once again from Section 3.1. Thereby, we can consider the strain energy function terms shown in Fig. 13*b* as the solution of the problem.

In Fig. 15 we show the axial stress distributions in the central section for each case under maximum load, from which we can obtain some feedback again. First, we can verify that the resulting stresses in the flat areas are almost coincident with the respective stresses for maximum load shown in Fig. 13*a*, so the respective maximum axial strains are correctly captured. Furthermore, the effective widths are again very similar to each other and they practicaly preserve their values with respect to the previous iteration. The reader can compare the effective widths shown in Figs. 6, 12 and 15 to verify that no relevant difference is appreciated. We conclude from these observations that a new iteration for both the effective lengths and the effective cross-sectional areas over the three directions is not needed, so we can take the values given in Eqs. (50) and (51) as the solution values for this skin disc specimen.

Finally, we show in Figs. 16, 17 and 18 the deformed configurations and axial stress fields under maximum load for the three simulations being performed. Remarkably, the loaded areas resemble those of the respective *uniaxial* tests over square (1:1) specimens due to the fact that the lateral restriction is very small at these deformation levels for skin, specially at 0° and 45°. As expected beforehand, the displacement field for the test at 45° is not symmetric, which justifies our use of the whole disc in the finite element model instead of performing the symmetries simplification in [16]. In the amplification of the border of the loading path shown in Fig. 18, it can be seen that there is a relevant (nonsymmetric) shear deformation due to the lack of coaxiality of the stress and strain tensor, an effect already commented above. However, once inside the loading path, it is also clearly seen that this shear deformation vanishes almost completely, an effect that is amplified by the 1:1 aspect ratio. This observation validates our original assumption that no relevant shear deformation was present in the loading zone in this test, and no iterations to correct this assumption are needed. Moreover, since the important loaded part of the specimen is maintaining a symmetric deformation, the observation also allows one to consider the symmetrized model of [16] as an excellent economical option for the purpose of determining the material parameters. Furthermore, in this case the part outside the loading path can also be neglected for additional computational savings and, remarkably, the little influence of the material outside the gauge zone in the overall behavior of the specimen shows a pathway for simple *in vivo* testing.

## 6. Conclusions

Soft biological tissues are complex composite multilayered specimens. Even the adequate determination of the stored energy for the purpose of performing finite element analysis in order to predict the behavior of the tissue in general loading conditions is extremely difficult. It is frequent the use of optimization algorithms and inverse analysis to obtain material parameters, which as extensively reported in the literature, result in a non-unique material behavior.

Given the natural variability of the mechanical behavior of skin, the experimental layout of Groves et al. [16] is of special interest because it allows to test the material behavior of the composite in several directions as to permit the characterization of a transversely isotropic material. We have analyzed the experiments through finite element simulations and obtained some relevant conclusions on the behavior of these tissues which we used to determine the WYPiWYG stored energy functions of the material. Even though the WYPiWYG approach is purely phenomenological, it is efficient for finite element simulations and it accurately predicts the behavior observed in the experiments of Groves et al. [16]. The proposed solution consists in the following steps: (1) assume homogeneous deformation and compute the corresponding stress-strain curves, (2) compute the WYPiWYG stored energies, (3) perform finite element nonhomogeneous simulations to compute effective lengths and cross-sections, (4) recompute the stress-strain curves with those effective values and (5) determine the final WYPiWYG stored energies to be used in any finite element simulation. In this case, no further iterations have been needed.

## Acknowledgments

Partial financial support for this work has been given by grant DPI2015-69801-R from the Dirección General de Proyectos de Investigación of the Ministerio de Economía y Competitividad of Spain. The ADINA program license used for this work has been a courtesy of ADINA R & D to the Universidad Politécnica de Madrid. FJM also acknowledges the support of the Department of Mechanical and Aerospace Engineering of University of Florida during the sabbatical period in which this paper was completed and Ministerio de Educación, Cultura y Deporte of Spain for the financial support for that stay under grant PRX15/00065.

## References


[1] M. Abbasi, M.S. Barakat, K. Vahidkhah, A.N. Azadani, Characterization of three-dimensional anisotropic heart valve tissue mechanical properties using inverse finite element analysis, J. Mech. Behav. Biomed. Mater. 62 (2016) 33–44.

[2] P. Agache, C. Monneur, J. Leveque, J. De Rigal, Mechanical properties and Young's modulus of human skin in vivo, Arch. Dermatol. Res. 269 (1980) 221–232.

[3] A.N. Annaidh, K. Bruyère, M. Destrade, M.D. Gilchrist, M. Otténio, Characterization of the anisotropic mechanical properties of excised human skin, J. Mech. Behav. Biomed. Mater. 5 (2012) 139–148.

[4] ASTM, 2009. E8/E8M, 2009. Standard test methods for tension testing of metallic materials. Technical Report. E0008-E0008M-09, ASTM international, West Conshohocken PA, 2009, ⟨http://www.astm.org⟩.

[5] J.E. Bischoff, E.M. Arruda, K. Grosh, Finite element modeling of human skin using an isotropic, nonlinear elastic constitutive model, J. Biomech. 33 (2000) 645–652.

[6] C. Bismuth, C. Gerin, E. Viguier, D. Fau, F. Dupasquier, L. Cavetier, L. David, C. Carozzo, The biomechanical properties of canine skin measured in situ by uniaxial extension, J. Biomech. 47 (2014) 1067–1073.

[7] G. Boyer, C. Pailler Mattei, J. Molimard, M. Pericoi, S. Laquieze, H. Zahouani, Non contact method for in vivo assessment of skin mechanical properties for assessing effect of ageing, Med. Eng. Phys. 34 (2012) 172–178.

[8] I.A. Brown, A scanning electron microscope study of the effects of uniaxial tension on human skin, Br. J. Dermatol. 89 (1973) 383–393.

[9] J. Crespo, M. Latorre, F.J. Montáns, WYPIWYG hyperelasticity for isotropic, compressible materials, Comput. Mech. 59 (1) (2017) 73–92.

[10] C.H. Daly, Biomechanical properties of dermis, J. Investig. Dermatol. (1982) 79.

[11] S.L. Evans, C.A. Holt, Measuring the mechanical properties of human skin in vivo using digital image correlation and finite element modelling, J. Strain Anal. Eng. Des. 44 (2009) 337–345.

[12] C. Flynn, A. Taberner, P. Nielsen, Measurement of the force-displacement response of in vivo human skin under a rich set of deformations, Med. Eng. Phys. 33 (2011) 610–619.

[13] T. Foutz, E. Stone, C. Abrams Jr, Effects of freezing on mechanical properties of rat skin, Am. J. Vet. Res. 53 (1992) 788–792.

[14] N.D. Gladkova, G. Petrova, N. Nikulin, S. Radenska-Lopovok, L. Snopova, Y.P. Chumakov, V. Nasonova, V. Gelikonov, G. Gelikonov, R. Kuranov, et al., In vivo optical coherence tomography imaging of human skin: norm and pathology, Skin. Res. Technol. 6 (2000) 6–16.

[15] C. Griffiths, J. Baker, T. Bleiker, R. Chalmers, D, C., Rooks Textbook of Dermatology, 4 vols, 9th Ed.´ Wiley-Blackwell, 2016.

[16] R.B. Groves, S.A. Coulman, J.C. Birchall, S.L. Evans, An anisotropic, hyperelastic model for skin: experimental measurements, finite element modelling and identification of parameters for human and murine skin, J. Mech. Behav. Biomed. Mater. 18 (2013) 167–180.

[17] R. Haut, The effects of orientation and location on the strength of dorsal rat skin in high and low speed tensile failure experiments, J. Biomech. Eng. 111 (1989) 136–140.

[18] F. Hendriks, D. Brokken, C. Oomens, F. Baaijens, Influence of hydration and experimental length scale on the mechanical response of human skin in vivo, using optical coherence tomography, Skin. Res. Technol. 10 (2004) 231–241.

[19] F. Hendriks, D. Brokken, C. Oomens, D. Bader, F. Baaijens, The relative contributions of different skin layers to the mechanical behavior of human skin in vivo using suction experiments, Med. Eng. Phys. 28 (2006) 259–266.

[20] E. ISO, 6892-1 metallic materials tensile testing part 1: method of test at room temperature. CEN Brussels, 2009.

[21] R.M. Jones, Mechanics of composite materials. vol. 193. Scripta Book Company Washington, DC, 1975.

[22] J. Jor, M. Nash, P. Nielsen, P. Hunter, Estimating material parameters of a structurally based constitutive relation for skin mechanics, Biomech. Model. Mechanobiol. 10 (2011) 767–778.

[23] A. Karimi, M. Navidbakhsh, M. Haghighatnama, A.M. Haghi, Determination of the axial and circumferential mechanical properties of the skin tissue using experimental testing and constitutive modeling, Comput. Methods Biomech. Biomed. Eng. 18 (2015) 1768–1774.

[24] Y. Kvistedal, P. Nielsen, Estimating material parameters of human skin in vivo, Biomech. Model. Mechanobiol. 8 (2009) 1–8.

[25] Y. Lanir, Y. Fung, Two-dimensional mechanical properties of rabbit skin. ii: experimental results, J. Biomech. 7 (1974) 171–182.

[26] M. Latorre, E. De Rosa, F.J. Montáns, Understanding the need of the compression branch to characterize hyperelastic materials, Int. J. Nonlinear Mech. 89 (2017) 14–24.

[27] M. Latorre, F.J. Montáns, Extension of the Sussman-Bathe spline-based hyperelastic model to incompressible transversely isotropic materials, Comput. Struct. 122 (2013) 13–26.

[28] M. Latorre, F.J. Montáns, What-you-prescribe-is-what-you-get orthotropic hyperelasticity, Comput. Mech. 53 (2014) 1279–1298.

[29] M. Latorre, F.J. Montáns, Anisotropic finite strain viscoelasticity based on the sidoroff multiplicative decomposition and logarithmic strains, Comput. Mech. 56 (2015) 503–531.

[30] M. Latorre, F.J. Montáns, Stress and strain mapping tensors and general work-conjugacy in large strain continuum mechanics, Appl. Math. Model. 40 (2016) 3938–3950.

[31] M. Latorre, E. Peña, F.J. Montáns, Determination and finite element validation of the WYPIWYG strain energy of superficial fascia from experimental data, Ann. Biomed. Eng. (2016) 1–12.

[32] M. Latorre, X. Romero, F.J. Montáns, The relevance of transverse deformation effects in modeling soft biological tissues, Int. J. Solids Struct. 99 (2016) 57–70.

[33] C. Li, G. Guan, R. Reif, Z. Huang, R. Wang, Determining elastic properties of skin by measuring surface waves from an impulse mechanical stimulus using phase-sensitive optical coherence tomography, J. R. Soc. Interface 9 (2012) 831–841.

[34] J. Lim, J. Hong, W.W. Chen, T. Weerasooriya, Mechanical response of pig skin under dynamic tensile loading, Int. J. Impact Eng. 38 (2011) 130–135.

[35] R. Marks, C. Edwards, The measurement of photodamage, Br. J. Dermatol. 127 (1992) 7–13.

[36] F.J. Montáns, J.M. Benítez, M.Á. Caminero, A large strain anisotropic elastoplastic continuum theory for nonlinear kinematic hardening and texture evolution, Mech. Res. Commun. 43 (2012) 50–56.

[37] M. Muñoz, J. Bea, J. Rodriguez, I. Ochoa, J. Grasa, A.P. del Palomar, P. Zaragoza, R. Osta, M. Doblaré, An experimental study of the mouse skin behaviour: damage and inelastic aspects, J. Biomech. 41 (2008) 93–99.

[38] R. Ogden, Large deformation isotropic elasticity: on the correlation of theory and experiment for incompressible rubberlike solids, in: Proceedings of the Royal Society of London A: Mathematical, Physical and Engineering Sciences, The Royal Society. pp. 565–584, 1972.

[39] C. Pailler-Mattei, S. Bec, H. Zahouani, In vivo measurements of the elastic mechanical properties of human skin by indentation tests, Med. Eng. Phys. 30 (2008) 599–606.

[40] C. Pailler-Mattei, R. Debret, R. Vargiolu, P. Sommer, H. Zahouani, In vivo skin biophysical behavior and surface topography as a function of ageing, J. Mech. Behav. Biomed. Mater. 28 (2013) 474–483.

[41] Y.S. Papir, K.H. Hsu, R.H. Wildnauer, The mechanical properties of stratum corneum: i. the effect of water and ambient temperature on the tensile properties of newborn rat stratum corneum, Biochim. Biophys. Acta – General. Subj. 399 (1975) 170–180.

[42] O. Pierron, D. Koss, A. Motta, Tensile specimen geometry and the constitutive behavior of Zircaloy-4, J. Nucl. Mater. 312 (2003) 257–261.

[43] D. Robertson, D. Cook, Unrealistic statistics: how average constitutive coefficients can produce non-physical results, J. Mech. Behav. Biomed. Mater. 40 (2014) 234–239.

[44] D.C. Schneider, T.M. Davidson, A.M. Nahum, In vitro biaxial stress-strain response of human skin, Arch. Otolaryngol. – Head. Neck Surg. 110 (1984) 329.

[45] O.A. Shergold, N.A. Fleck, D. Radford, The uniaxial stress versus strain response of pig skin and silicone rubber at low and high strain rates, Int. J. Impact Eng. 32 (2006) 1384–1402.

[46] P. Skacel, J. Bursa, Poisson's ratio of arterial wall-Inconsistency of constitutive models with experimental data, J. Mech. Behav. Biomed. Mater. 54 (2016) 316–327.

[47] T. Sussman, K.J. Bathe, A model of incompressible isotropic hyperelastic material behavior using spline interpolations of tension-compression test data, Commun. Numer. Methods Eng. 25 (2009) 53–63.

[48] L. Tian, J. Henningsen, M.R. Salick, W.C. Crone, M. Gunderson, S.H. Dailey, N.C. Chesler, Stretch calculated from grip distance accurately approximates mid-specimen stretch in large elastic arteries in uniaxial tensile tests, J. Mech. Behav. Biomed. Mater. 47 (2015) 107–113.

[49] D. Veronda, R. Westmann, Mechanical characterization of skin-finite deformations, J. Biomech. 3 (1970) 111–124.

[50] A.W. Wan, Biaxial tension test of human skin in vivo, Bio-Med. Mater. Eng. 4 (1993) 473–486.

[51] Y. Wang, K. Marshall, Y. Baba, G. Gerling, L. EA, Hyperelastic metarial properties of mouse skin under compression, Plos One 8 (2013) 1–9.

[52] J. Weickenmeier, M. Jabareen, E. Mazza, Suction based mechanical characterization of superficial facial soft tissues, J. Biomech. 48 (2015) 4279–4286.

[53] J.A. Weiss, B.N. Maker, S. Govindjee, Finite element implementation of incompressible, transversely isotropic hyperelasticity, Comput. Methods Appl. Mech. Eng. 135 (1996) 107–128.

[54] R.H. Wildnauer, J.W. Bothwell, A.B. Douglass, Stratum corneum biomechanical properties i. influence of relative humidity on normal and extracted human stratum corneum, J. Investig. Dermatol. 56 (1971) 72–78.

[55] F. Xu, K. Seffen, T. Lu, Temperature-dependent mechanical behaviors of skin tissue, IAENG Int. J. Comput. Sci. 35 (2008) 92–101.